Aluminum Properties and Physical Metallurgy
John E. Hatch editor, p 58-104
DOI: 10.1361/appm1984p058

CHAPTER 3

MICROSTRUCTURE OF ALLOYS*

The examination of microstructure is one of the principal means of evaluating alloys and products to determine the effects of various fabrication and thermal treatments, evaluate the effects of new procedures, and analyze the cause of failures. A compilation of typical and atypical micrographs is presented in Ref 1. Reference 2 discusses general preparation techniques for aluminum metallographic samples. Phase diagrams and identification of constituents, important to the interpretation of structures, are covered in Ref 2 and 3.

Many of the changes that become apparent with the examination of aluminum macrostructure and microstructure occur simultaneously with the freezing, homogenization, preheat, hot or cold reduction, annealing, or solution or precipitation heat treatment of the aluminum alloy. Good interpretation of microstructure relies on having a complete history of the sample for analysis. Although this is not always possible, the more information available, the more reliable the interpretation. Comparative samples with known histories are helpful in any given examination.

As a general rule, examination should start at normal vision level and proceed to higher magnification, according to the need for more detailed interpretation. This also permits better choice of sample location, for at higher magnification, the sample area becomes extremely small. Simplicity and cost make optical methods of macro- and micro-examination the most useful. Limited depth of field and magnification dictate the use of electron microscopy in areas where fine structure or depth of field are important. Electron techniques supplement and in some cases replace the selective use of etchants, and they enable the determination of microchemical analysis, which contributes to more conclusive answers.

Examination of fracture surfaces is essential to determine the mode and direction of crack propagation. Key fractographic features are usually not visible to the unaided eye and can be seen clearly only when magnified. Good analysis requires care in handling specimens to avoid contaminating the fracture surface before examination. Three techniques are commonly used to determine if a fracture occurred by fatigue, ultimate tensile rupture, or stress-corrosion cracking and other modes. These methods are (1) optical microscopy, (2) transmission electron microscopy replica methods (TEM), and (3) scanning electron microscopy (SEM).

Transmission electron microscopy replica methods are well established and widely used (Ref 4). The replica method involves making a thin,

*This chapter was revised by a team comprised of R.E. Hughes and S.A. Levy, Reynolds Metals Co.; A.T. Thomas and M.D. Ball, Alcan International Ltd.; P.R. Sperry, Consolidated Aluminum Corp.; A.G. Miller, W.H. Graham, and E.A. Ledbury, Boeing Commercial Airplane Co.; and F.M. Krill, Kaiser Aluminum & Chemical Corp. The original chapter was authored by M.S. Hunter, A.M. Montgomery, and G.W. Wilcox, Aluminum Company of America.

accurate replica of a portion of the fracture surface. Transmission electron microscopy is used to view the replica of the surface to determine fracture mode. Transmission electron microscopy replica methods offer a higher magnification range than optical microscopes with well-focused images at all magnifications. Typical TEM magnifications are 600 to 10,000 diameters. Handbooks of fracture surface appearances have been published for many alloy systems. Thus, a good database of information is available for analysis.

Some disadvantages of TEM replica methods include: (1) long specimen preparation time, (2) selective specimen sampling plan because typical replicas must fit onto a 3-mm (0.1-in.) grid, (3) artifacts in the replica that may occur during specimen preparation, and (4) unavailability of microchemical information for identification of chemical microheterogeneities. Thin foil techniques normally are used in TEM examination. Examples are given in the TEM section of this chapter.

Scanning electron microscopy of fracture surfaces is a newer process than both TEM and optical microscopy. The database of SEM fracture surfaces is much more limited than TEM methods. However, because of the flexibility of SEM, these techniques are expected to become the method of choice for most analyses.

LIGHT MICROSCOPY OF WROUGHT ALLOYS

Light microscopy is the major tool for microstructural determination of aluminum alloys and is recommended for use before electron optics. It is useful up to magnifications of about 1500× where features as small as 0.1 μm (0.004 mil) can be resolved. Light microscopy identifies most second-phase particles of sufficient size (>1 μm, or >0.04 mil), shows the size and distribution of resolvable particles, and shows the state of the grain or crystal structure of the aluminum or solid solution matrix. It can also show features such as cladding thickness and diffusion, type and depth of corrosive attack, partial melting because of overheating, and the presence of extraneous nonmetallic inclusions or unduly coarse intermetallic phases. Light microscopy does not reveal precipitate particles that are responsible for precipitation hardening, nor does it reveal dislocation arrangements; sometimes, etching or preparation effects can be used to infer conclusions about these conditions. Generally, analysis of these conditions is in the domain of electron microscopy.

The identification of elemental or intermetallic phases is an important part of a light microscopy examination. These phases are the consequence of equilibrium or nonequilibrium reactions and changes occurring within a given alloy because of casting conditions, mechanical working, and thermal treatment. The phases are related to the equilibrium or constitution diagrams for binary, ternary, quaternary, or even more complex systems (Ref 2 and 3). The crystal structure and compositional makeup of such phases have been determined, and means of identifying them by optical characteristics or etching behavior are known. See *Metals Handbook* for more information (Ref 2). For nonstandard specimens or where some ambiguity exists, optical examination can be supplemented or replaced by electron probe microanalysis or electron diffraction methods, which normally allow a precise identification to be made.

Conventionally produced wrought aluminum alloys originate from a cast ingot from which all subsequent mechanical and thermal processing represents varying degrees of change to the as-cast structure. Modifications are relatively minor for large wrought forms such as forgings, thick plate, and heavy extrusions that are hot worked. They become greater as the total amount of reduction in original cross-sectional area is increased by hot and cold working and as the frequency of thermal treatments, such as annealing and solution heat treating, is increased. The visible modifications consist of the following:

- Alteration of the composition and crystal structure of phases because of peritectic reactions that were suppressed during casting
- Solution of more soluble phases and spheroidization and coalescence to reduce their surface energy
- Elevated-temperature precipitation of elements that had supersaturated the as-cast solid solution
- Mechanical fragmentation of brittle intermetallic phases and alignment of these particles in the principal direction of working
- Deformation of the original cast grain matrix and subsequent recovery or recrystallization

For other processes such as powder metallurgy, the microstructure is dependent on the method of manufacturing the powders and compacting and sintering the finished pieces (Chapter 10 in this Volume).

Wrought alloys are divided into seven major classes according to their principal alloy elements. Each class represents a different type of microstructure because of these alloy differences. Typical microstructural features are described in this chapter for each class and show how microstructure progressively develops from the as-cast ingot to the final wrought form. Furthermore, alloy classes can be divided into two categories according to whether they are strengthened by work hardening only or by heat treatment (precipitation hardening). The former applies to 1XXX, 3XXX, 4XXX, and 5XXX alloys, while the latter applies to 2XXX, 6XXX, and 7XXX alloys.

1XXX or Commercially Pure Aluminum. Because iron and silicon are ever-present impurity elements and the solid solubility of iron in aluminum is very small, phases of aluminum-iron or aluminum-iron-silicon are seen in microstructures of all but refined, super-purity aluminum. In the as-cast condition, all of the phases that come into equilibrium with aluminum may be found—$FeAl_3$, Fe_3SiAl_{12}, or $Fe_2Si_2Al_9$. In addition, a number of metastable nonequilibrium phases may be formed when solidification is rapid. $FeAl_6$, a phase that has the same crystal structure as $MnAl_6$, is one example (Ref 5 and 6). Minor impurity or addition elements such as copper and manganese that are not in sufficient quantity to form their own phases influence the type and quantity of less stable phases. High resolution and sophisticated identification techniques are required to identify these phases. Subsequent thermal processes generally revert these phases back to the equilibrium types.

1100 Alloy. Figure 1 shows the typical constituent in as-cast 1100 aluminum; Fig. 2 shows the effect of a high-temperature treatment before working; and Fig. 3 shows redistributed constituent in a typical worked

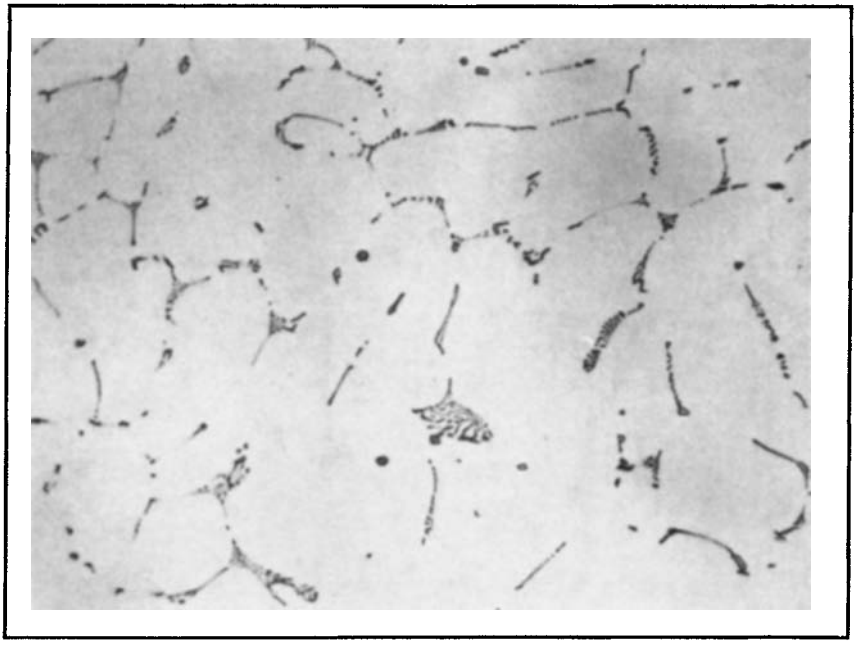

Fig. 1. 1100 as-cast ingot showing the typical constituent, predominantly Fe_3SiAl_{12}, in the dendrite interstices. 0.5% hydrofluoric acid, 455×. (Courtesy of Kaiser Aluminum & Chemical Corp.)

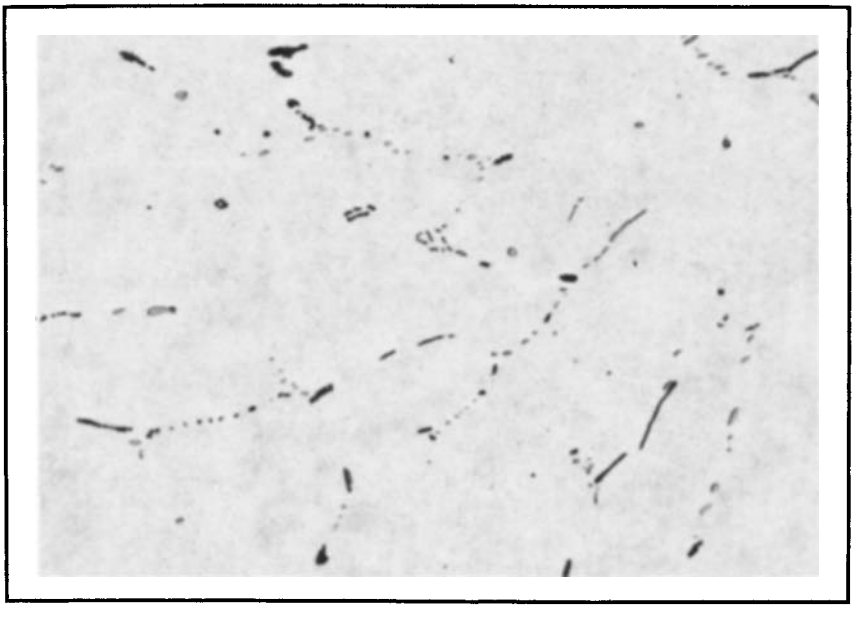

Fig. 2. 1100 homogenized ingot showing the effect of heating on the microstructure. A portion of the Fe_3SiAl_{12}, (light) has reverted to $FeAl_3$ (dark). 20% sulfuric acid, 455×. (Courtesy of Kaiser Aluminum & Chemical Corp.)

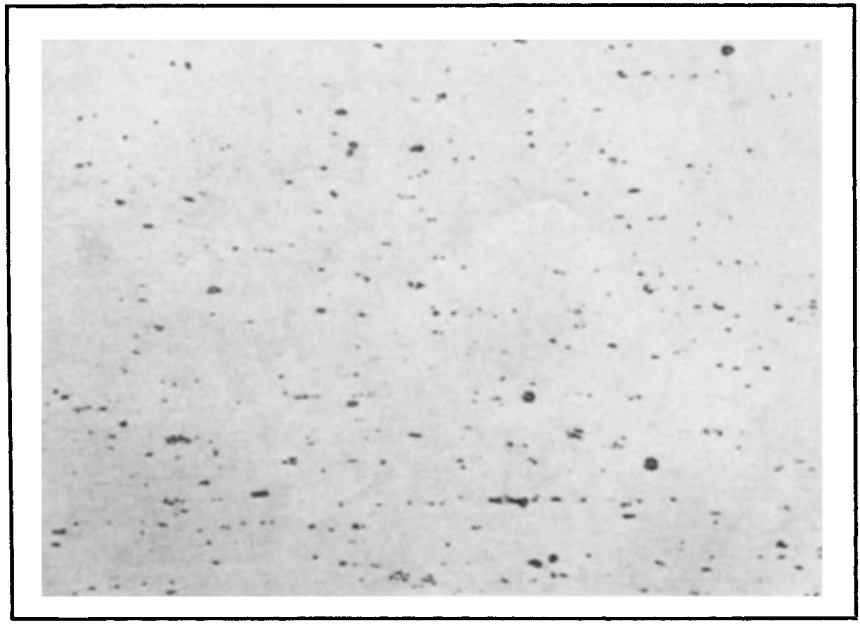

Fig. 3. 1100 sheet showing fragmented and redistributed constituent as a result of mechanical working. 0.5% hydrofluoric acid, 455×. (Courtesy of Kaiser Aluminum & Chemical Corp.)

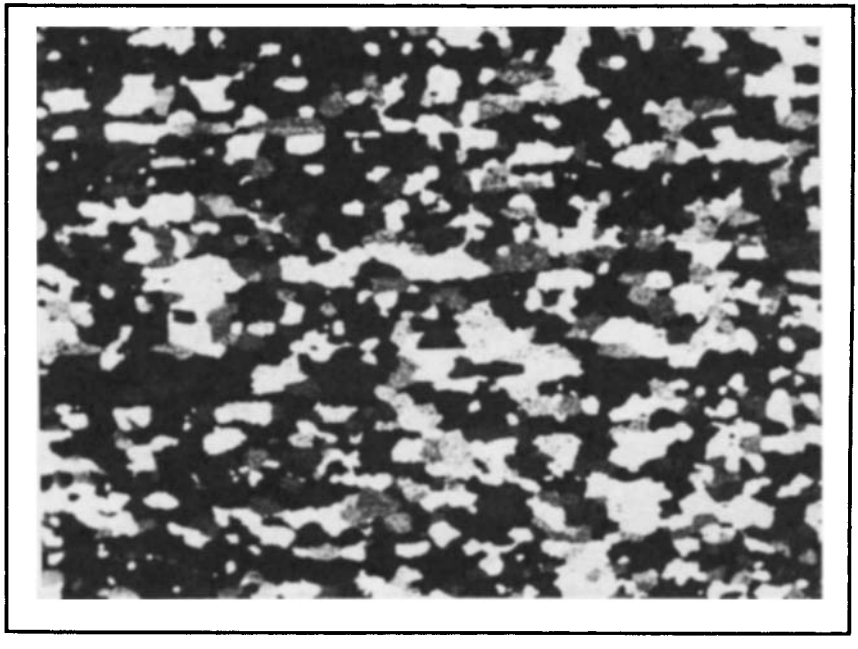

Fig. 4. 1100 sheet showing slightly elongated annealed grain structure. Barker's electrolytic etch, 90×. (Courtesy of Kaiser Aluminum & Chemical Corp.)

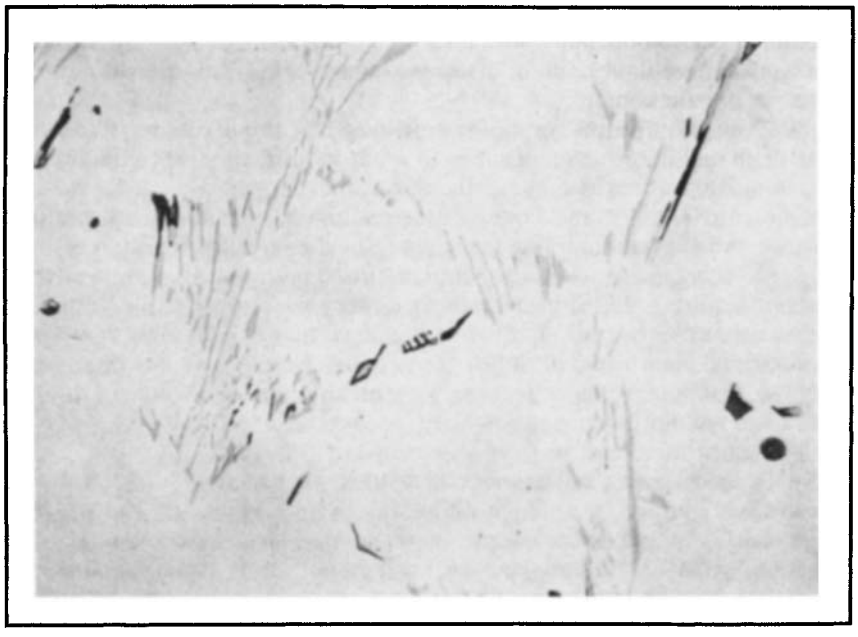

Fig. 5. 3003 as-cast ingot showing the distribution of predominantly $(Mn,Fe)Al_6$ (light) and $(Fe,Mn)_3SiAl_{12}$ (dark) at dendrite interstices. 10% phosphoric acid, 455×. (Courtesy of Kaiser Aluminum & Chemical Corp.)

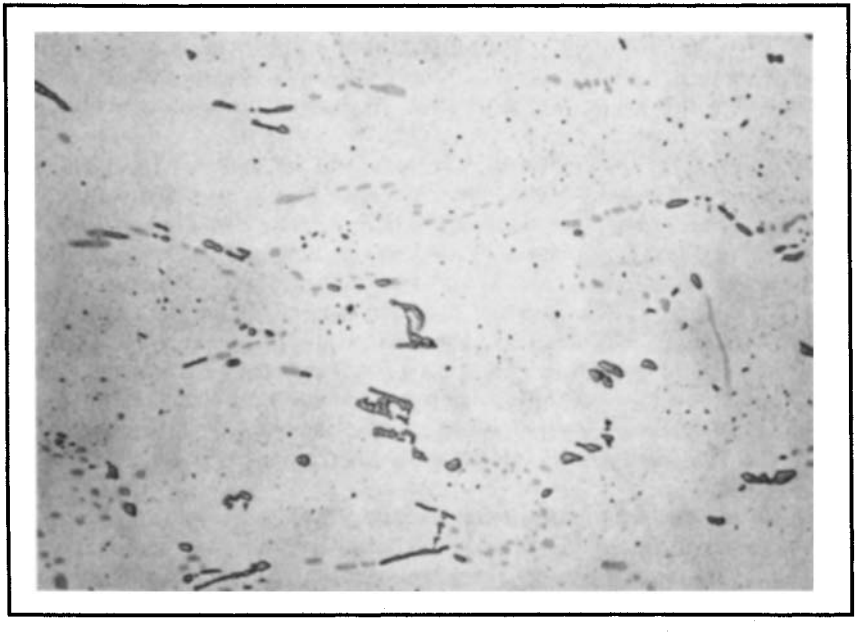

Fig. 6. 3003 homogenized ingot showing transformation to the predominantly $(Fe,Mn)_3SiAl_{12}$ phase by a delayed peritectic reaction. 10% phosphoric acid, 455×. (Courtesy of Kaiser Aluminum & Chemical Corp.)

structure. The grain structure of annealed sheet (Fig. 4) shows a slight departure from equiaxiality because of alignment of iron-rich particles. The apparent volume fraction of second-phase particles is almost a direct function of iron content.

3XXX or Aluminum-Manganese Alloys. The popular alloy 3003 consists of the addition of manganese to what is basically 1100 aluminum. The dominant phases become $(Mn,Fe)Al_6$ and $(Fe,Mn)_3SiAl_{12}$. In the as-cast structure (Fig. 5), the former phase predominates; subsequent heating causes a transformation to the latter phase by a delayed peritectic reaction (Fig. 6). Manganese also supersaturates the cored solid solution of the primary dendrites and subsequently precipitates as a dispersoid (Fig. 7). Grains formed by annealing of work-hardened material are more flattened or elongated than those of 1100, principally because of the dispersoid (Fig. 8). Some manganese remains in solid solution. A few alloys in this class also contain magnesium which, because of its affinity for silicon, tends to shift the phase proportioning toward $(Mn,Fe)Al_6$.

5XXX or Aluminum-Magnesium Alloys. Magnesium is largely present in solid solution in wrought alloys, but it appears as eutectic Mg_2Al_3 in increasing amounts in as-cast ingots as the magnesium content increases (Fig. 9). In the same manner, magnesium forms increasing amounts of Mg_2Si, but the solubility of this phase is reduced so that a certain amount may remain out of solution and visible in wrought products (Fig. 10). When magnesium content exceeds about 3.5%, Mg_2Al_3 or metastable Mg_2Al_3' may precipitate in grain boundaries or within grains, resulting from low-temperature thermal operations (Fig. 11). Chromium is a frequent additive and may appear as a fine dispersoid of $Cr_2Mg_3Al_{18}$. When manganese also is present, iron-rich phases become quite complex, and $MnAl_6$, probably containing some chromium, appears as a dispersoid. Cold working of aluminum-magnesium alloys produces prominent deformation bands that are decorated by magnesium-rich precipitates (Fig. 12).

4XXX or Aluminum-Silicon Alloys. Except for some architectural applications and forged pistons, most wrought 4XXX alloys are used for welding and brazing filler materials where they are remelted. However, good joining characteristics may depend on having a uniform and fine initial wrought structure. The as-cast phases are usually elemental silicon and $Fe_2Si_2Al_9$ (Fig. 13). Thermal treatment causes silicon to coalesce and spheroidize (Fig. 14), while the insoluble iron-rich phase is not altered. Figure 15 shows a 4343 clad layer on a 3003 core used for brazing sheet, and Fig. 16 shows a bare 3003 fin brazed to this clad sheet. Because of interalloying between the two alloys, needle-like $Fe_2Si_2Al_9$ is replaced by polygonal $(Fe,Mn)_3SiAl_{12}$. Interalloying also changes the constitution of weld beads.

6XXX or aluminum-magnesium-silicon alloys are formulated to make use of the solubility of Mg_2Si and thereby utilize precipitation hardening. If there is no manganese or chromium present, the iron-rich phases are Fe_3SiAl_{12}, $Fe_2Si_2Al_9$, or a mixture of the two, depending on the proportions of magnesium, silicon, and iron. Manganese and chromium stabilize $(Fe,Mn,Cr)_3SiAl_{12}$. In dilute alloys such as 6063, heating the cast structure (Fig. 17) to moderate temperatures dissolves all Mg_2Si (Fig. 18).

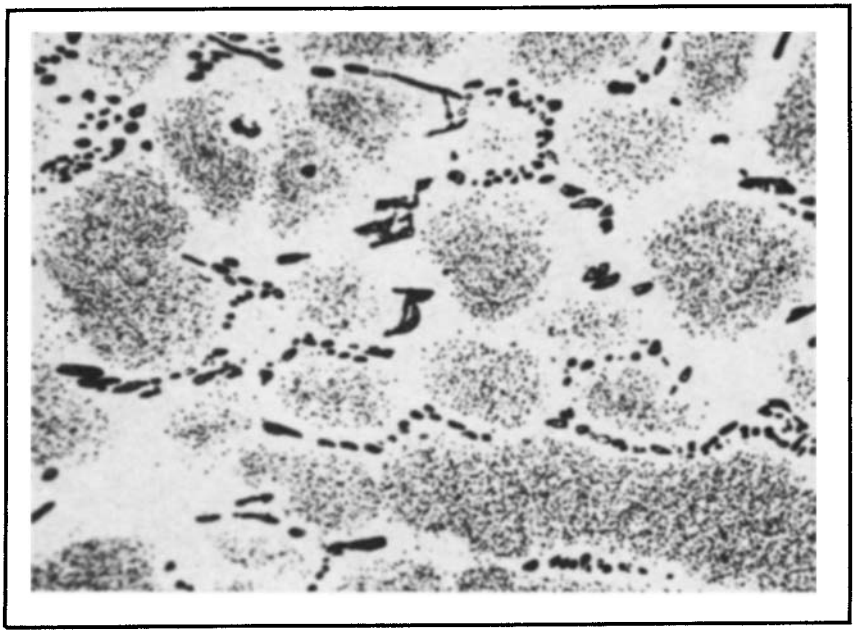

Fig. 7. 3003 homogenized ingot, similar to Fig. 6 but etched to reveal dispersoid precipitate in the primary aluminum dendrite matrix. 0.5% hydrofluoric acid, 455×. (Courtesy of Kaiser Aluminum & Chemical Corp.)

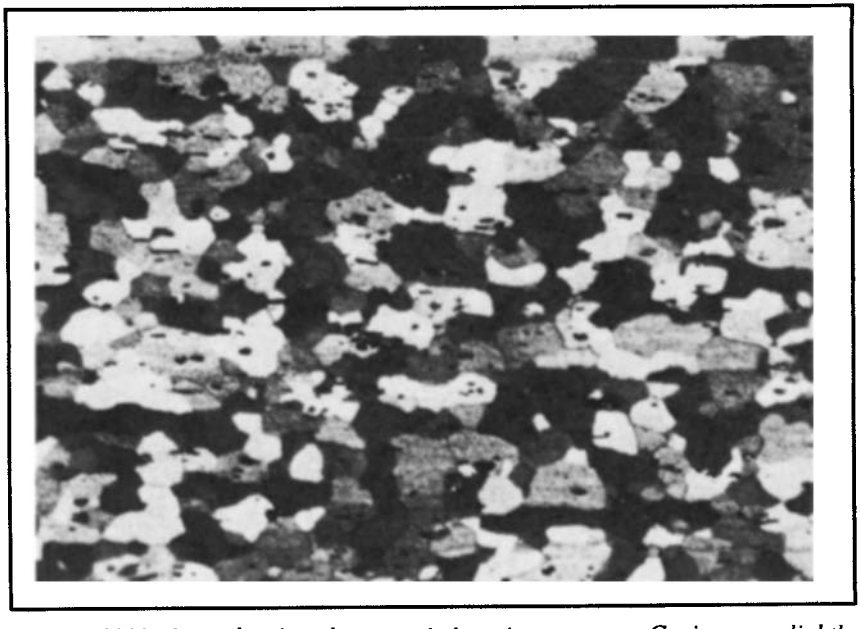

Fig. 8. 3003 sheet showing the annealed grain structure. Grains are slightly elongated because of the dispersoid. Barker's electrolytic etch, 260×. (Courtesy of Kaiser Aluminum & Chemical Corp.)

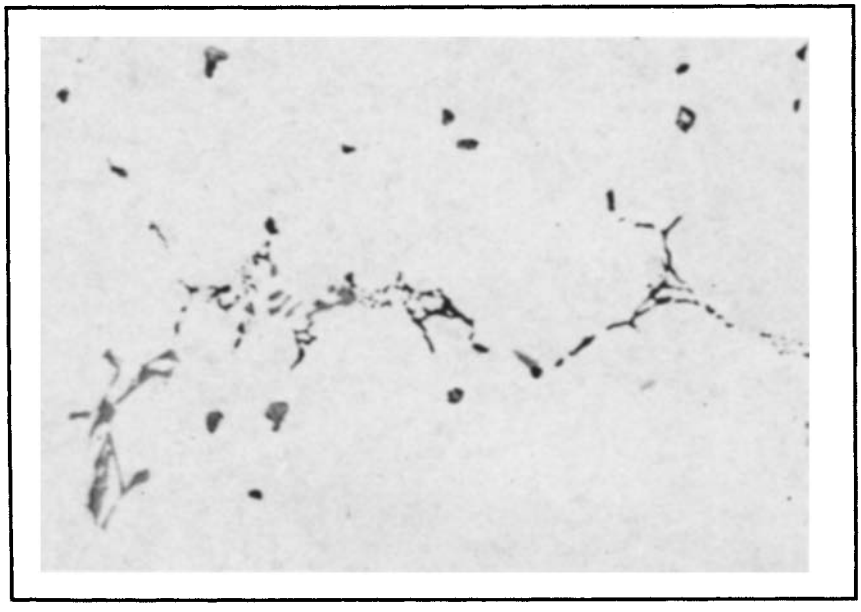

Fig. 9. 5056 as-cast ingot showing $(Fe,Cr)_3SiAl_{12}$ (gray), Mg_2Si (dark), and Mg_2Al_3 (mottled, outlined) in dendrite interstices. 0.5% hydrofluoric acid, 435×. (Courtesy of Kaiser Aluminum & Chemical Corp.)

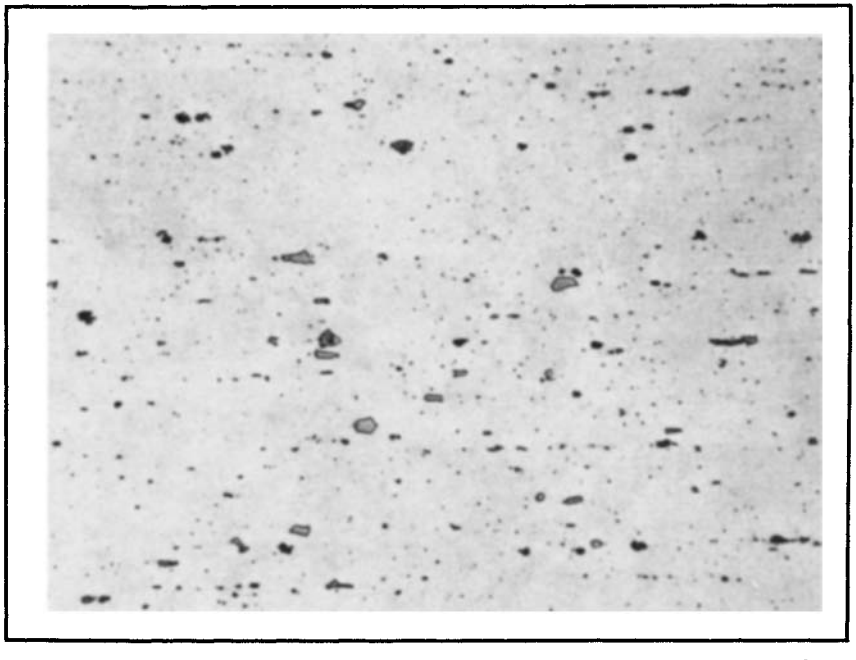

Fig. 10. 5052 sheet showing the fragmented, more uniform distribution of the constituent particles consisting of $(Fe,Cr)_3SiAl_{12}$ (light) and Mg_2Si (dark). 0.5% hydrofluoric acid, 455×. (Courtesy of Kaiser Aluminum & Chemical Corp.)

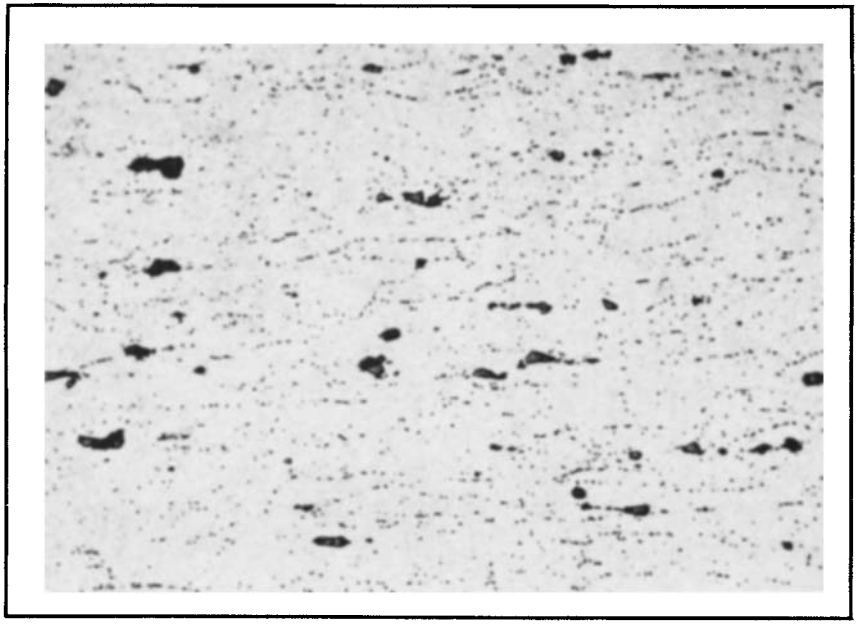

Fig. 11. 5086-H34 cold rolled and stabilized sheet showing the constituent distribution and discontinuous Mg_2Al_3 grain boundary precipitate. 10% phosphoric acid, 455×. (Courtesy of Kaiser Aluminum & Chemical Corp.)

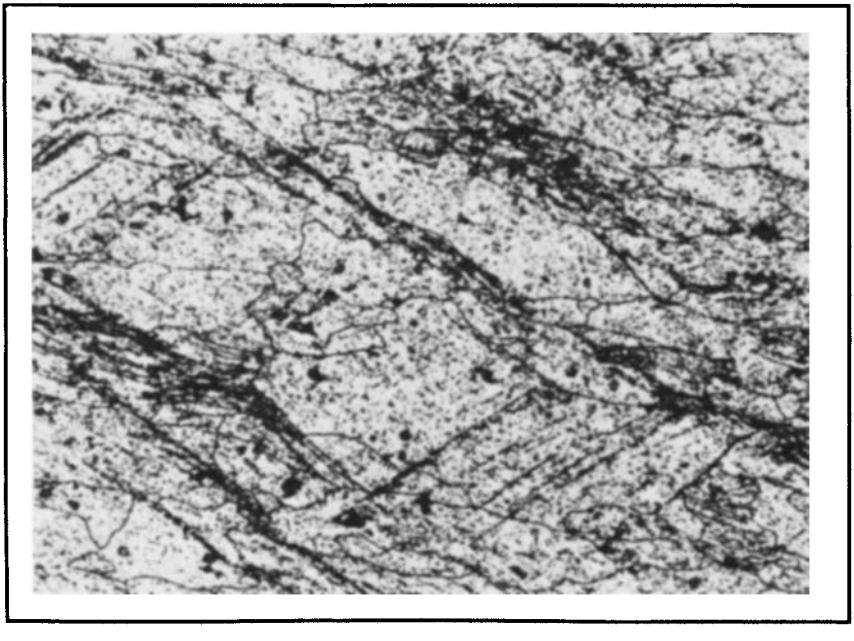

Fig. 12. 5083 cold forged stock, heated 24 h at 120 °C (250 °F), showing Mg_2Al_3 precipitate on deformation bands. 10% phosphoric acid, 445×. (Courtesy of Kaiser Aluminum & Chemical Corp.)

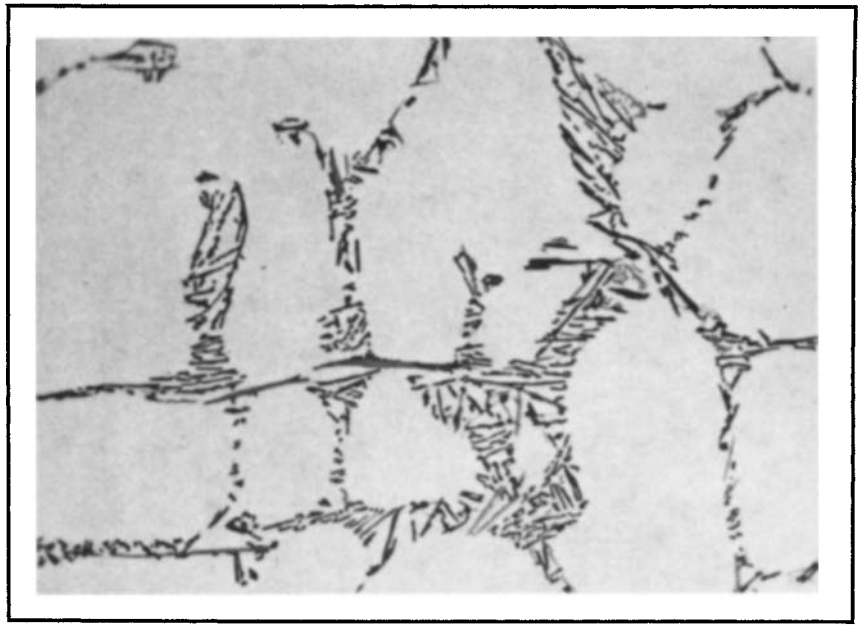

Fig. 13. 4043 as-cast ingot with $Fe_2Si_2Al_9$ (light) and silicon (dark) in dendrite interstices. 0.5% hydrofluoric acid, 455×. (Courtesy of Kaiser Aluminum & Chemical Corp.)

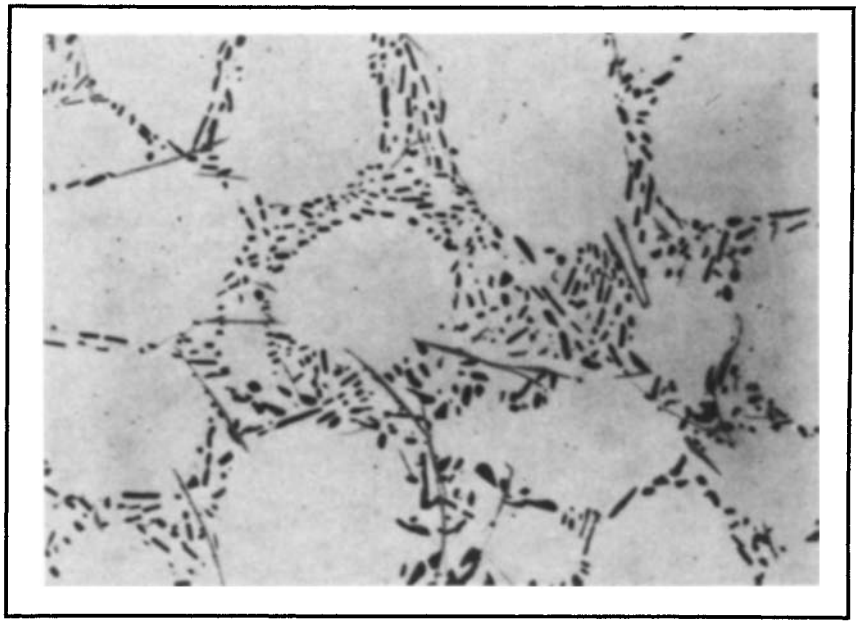

Fig. 14. 4043 homogenized ingot showing rounding and coalescence of the silicon constituent with the insoluble iron-rich phase remaining unchanged. 0.5% hydrofluoric acid, 445×. (Courtesy of Kaiser Aluminum & Chemical Corp.)

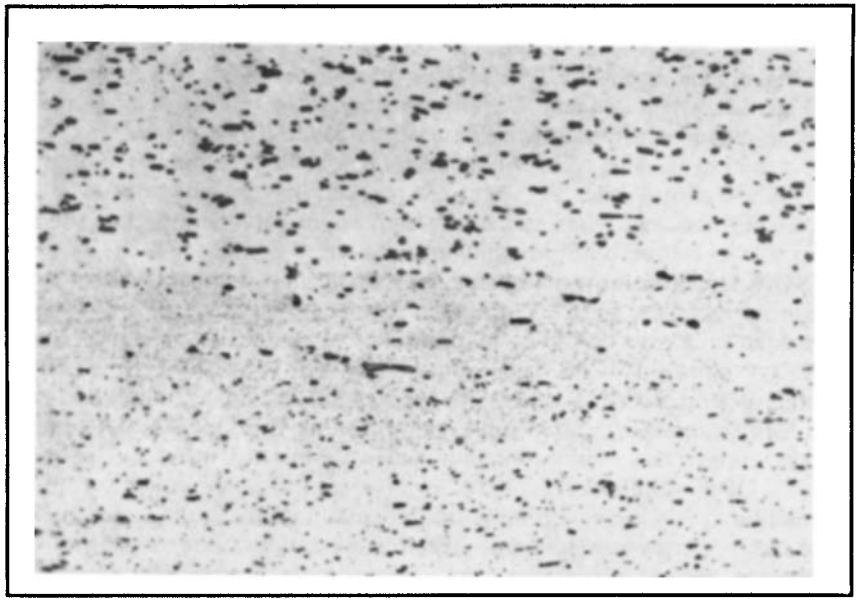

Fig. 15. No. 12 brazing sheet—4343 clad on 3003 core, showing the spheroidized silicon particles in the cladding (upper portion). 0.5% hydrofluoric acid, 225×. (Courtesy of Kaiser Aluminum & Chemical Corp.)

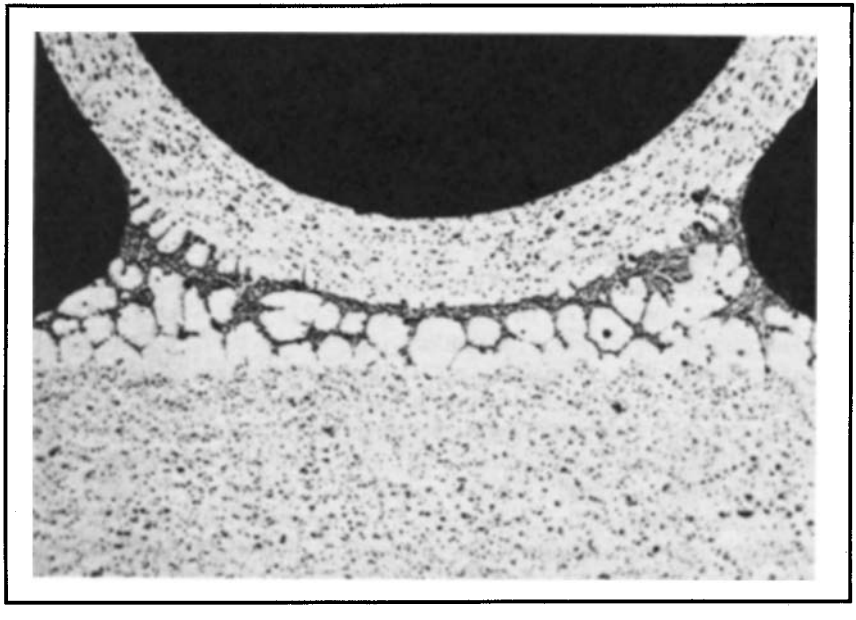

Fig. 16. 3003 bare fin brazed to a No. 12 brazing sheet showing that the 4343 has reverted to a cast dendritic structure, with some interalloying. 0.5% hydrofluoric acid, 90×. (Courtesy of Kaiser Aluminum & Chemical Corp.)

More highly alloyed 6061 generally has an excess of Mg_2Si at the solutionizing temperature and, if slowly cooled, precipitates in a Widmænstatten form (Fig. 19). Solution heat treated 6061 appears as shown in Fig. 20, where T4 and T6 tempers cannot be readily distinguished. Special etching techniques can be used to make a distinction (Fig. 21), but it is best to have a known standard to use for comparison. Some of the 6XXX alloys used for electrical conductivity are put into an overaged condition and, when etched, exhibit a light band along grain boundaries that is caused by a precipitate-free zone (Fig. 22).

2XXX or aluminum-copper alloys are usually complex because of the many additives used for strength, corrosion resistance, or grain structure control. Alloy 2024, with aluminum + copper + magnesium + manganese + iron + silicon, has a multiphase ingot structure (Fig. 23) consisting of $(Mn,Fe)_3SiAl_{12}$, Mg_2Si, $CuAl_2$, and Al_2CuMg, and occasional $(Fe,Mn)Al_3$ or $(Mn,Fe)Al_6$. Subsequent heating (Fig. 24) dissolves much of the copper and magnesium but leaves some Al_2CuMg and perhaps $CuAl_2$ out of solution. All of the iron-containing phases undergo transformation to Al_7Cu_2Fe, possibly accompanied by other minor phases. Simultaneously, manganese is precipitated from solid solution as $Cu_2Mn_3Al_{20}$ dispersoid. Slow cooling causes Al_2CuMg to precipitate in a Widmænstatten pattern.

The normal wrought 2024-T4 product shows rounded Al_2CuMg as an undissolved excess phase, irregularly shaped particles of unreacted $(Mn,Fe)_3SiAl_{12}$ and reaction product Al_7Cu_2Fe, along with fine dispersoid of $Cu_2Mn_3Al_{20}$ (Fig. 25). The latter causes grains formed during solution heat treatment to be moderately elongated or flattened. Grain contrast in copper-rich alloys is obtained by a combination of etch pitting and redeposition of copper on the more rapidly dissolved grain orientations (Fig. 26). This etching characteristic is useful to indicate when there has been excessive diffusion of copper into the pure aluminum cladding on sheet. Magnesium is also diffused, although this diffusion is not as readily revealed by light microscopy.

Alloy 2014 differs from 2024 in that the magnesium content is less and the silicon content is higher. The high silicon stabilizes $(Mn,Fe)_3SiAl_{12}$ as the only iron-rich phase. $CuAl_2$ and a quaternary phase, $Cu_2Mg_8Si_6Al_5$, are the soluble phases and $Cu_2Mn_3Al_{20}$ dispersoid is probably augmented by Mn_3SiAl_{12} coming out of solution (Fig. 27). The higher dispersoid concentration and pronounced banding inherited from the cast structure may result in highly elongated, recrystallized grains (Fig. 28).

Alloy 2011 is simpler in composition (aluminum + copper + iron + silicon), except for the addition of lead and bismuth to improve machinability. The phases after solidification and after thermal treatment are Al_7Cu_2Fe (insoluble) and $CuAl_2$ (usually some in excess of solid solubility). The lead-bismuth liquid phase first separates out in the dendrite interstices while solidification is in progress, then completes its solidification at a very low temperature. It spheroidizes during solution heat treatment and has a complex structure when resolidified during quenching (Fig. 29).

Because solution heat treatment temperatures are close to the equilibrium solidus in 2XXX alloys, overheating is a hazard that requires mi-

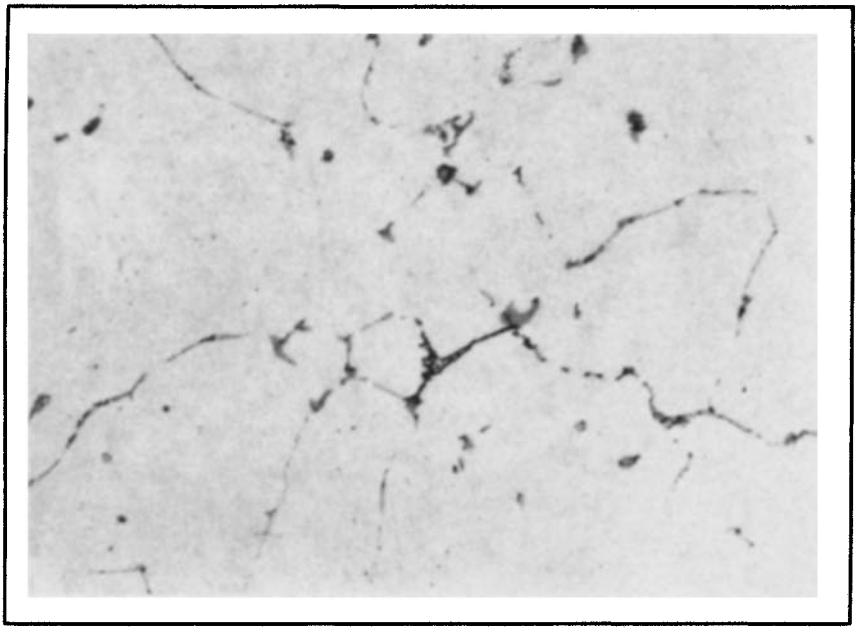

Fig. 17. 6063 as-cast ingot showing iron-rich phases (light) and Mg_2Si (dark) in dendrite interstices. 0.5% hydrofluoric acid, 445×. (Courtesy of Kaiser Aluminum & Chemical Corp.)

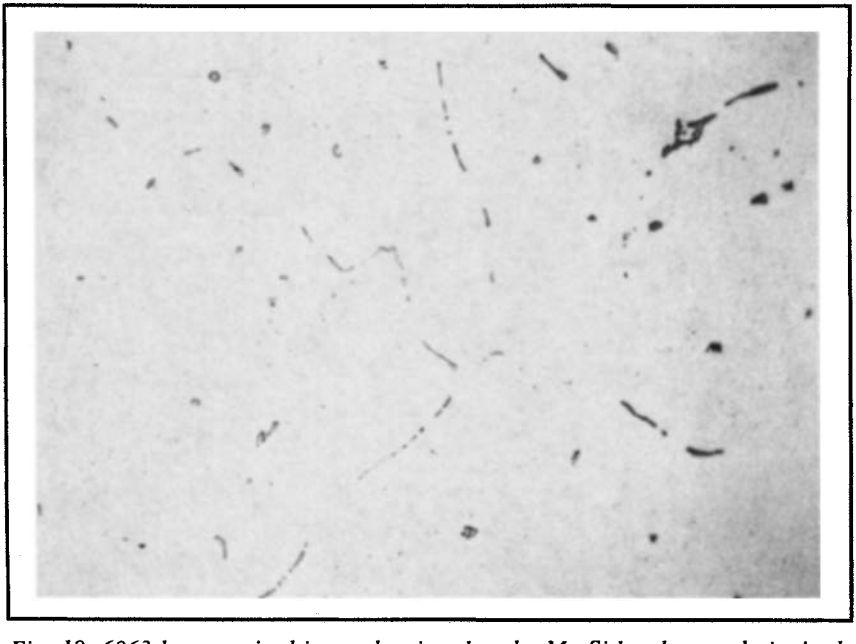

Fig. 18. 6063 homogenized ingot showing that the Mg_2Si has been solutionized, leaving only slightly spheroidized iron-rich phases. 0.5% hydrofluoric acid, 445×. (Courtesy of Kaiser Aluminum & Chemical Corp.)

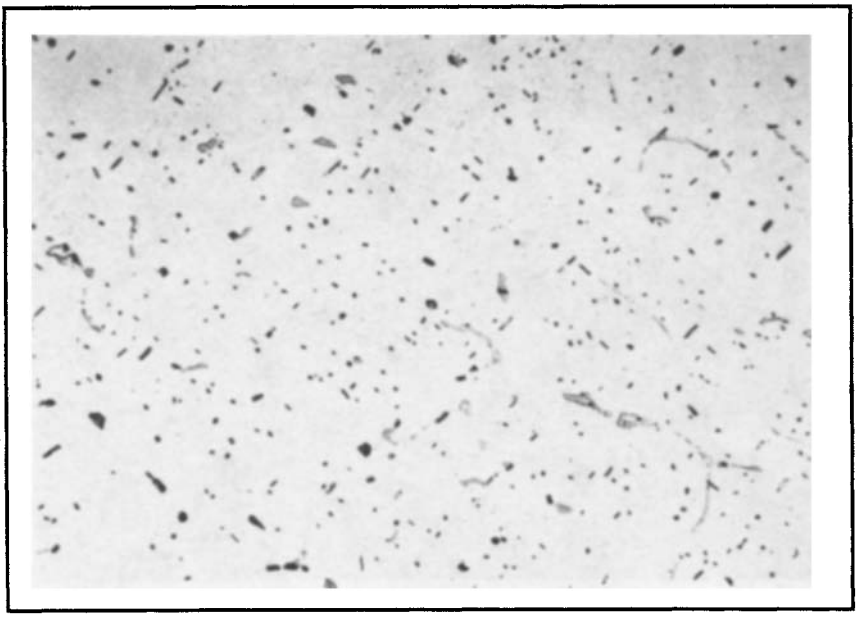

Fig. 19. 6061 homogenized ingot showing some undissolved Mg_2Si and some Mg_2Si reprecipitation during cooling in a Widmænstatten pattern. 0.5% hydrofluoric acid, 455×. (Courtesy of Kaiser Aluminum & Chemical Corp.)

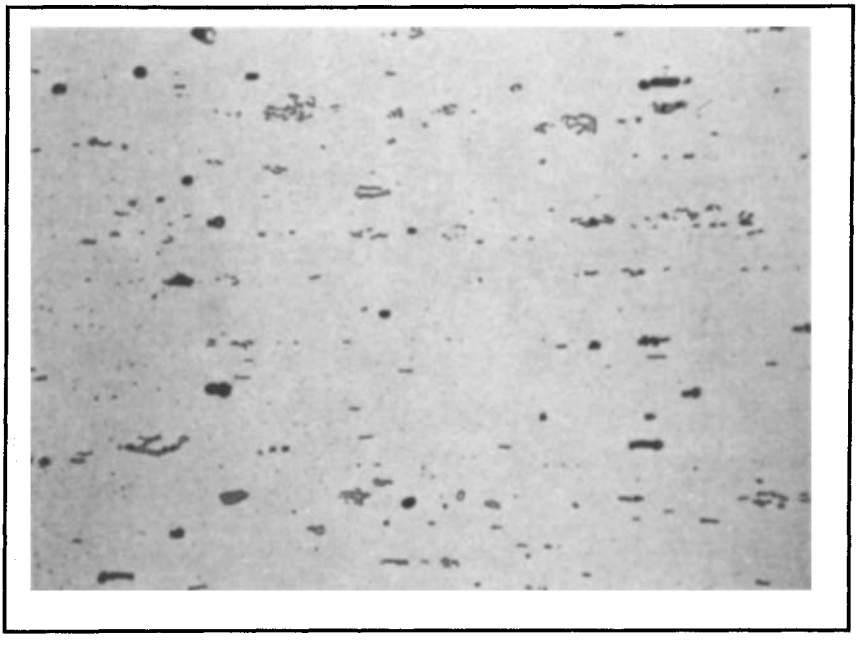

Fig. 20. 6061-T6 sheet showing insoluble $(Fe,Cr)_3SiAl_{12}$ and excess soluble Mg_2Si particles (dark) as redistributed by mechanical working. 0.5% hydrofluoric acid, 455×. (Courtesy of Kaiser Aluminum & Chemical Corp.)

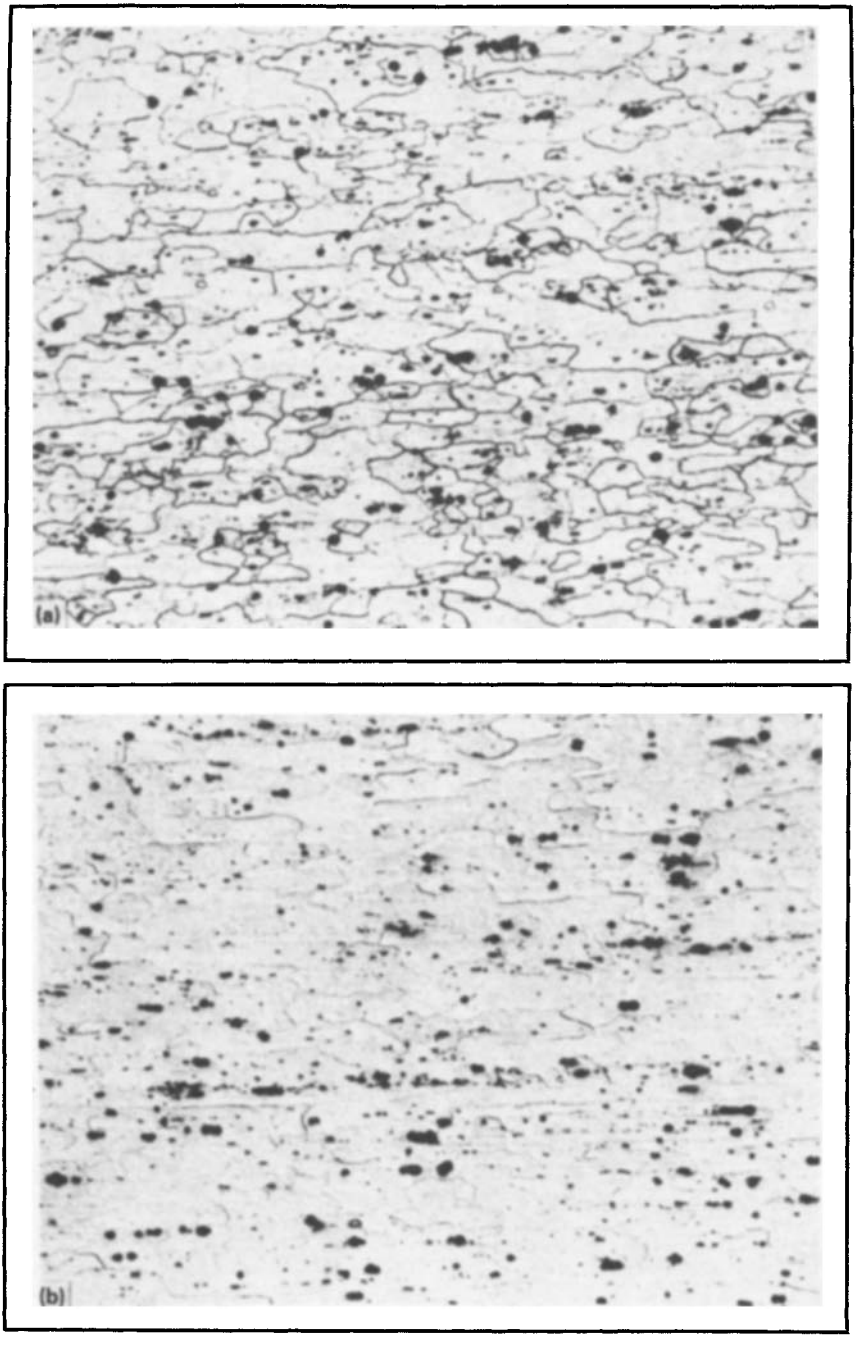

Fig. 21. 6061-T4(a) and T6(b) sheet showing the typical constituent distribution and loss of clear grain delineation caused by Mg_2Si precipitation from artificial aging. Hydrofluoric acid and sulfuric acid, 230×. (Courtesy of Kaiser Aluminum & Chemical Corp.)

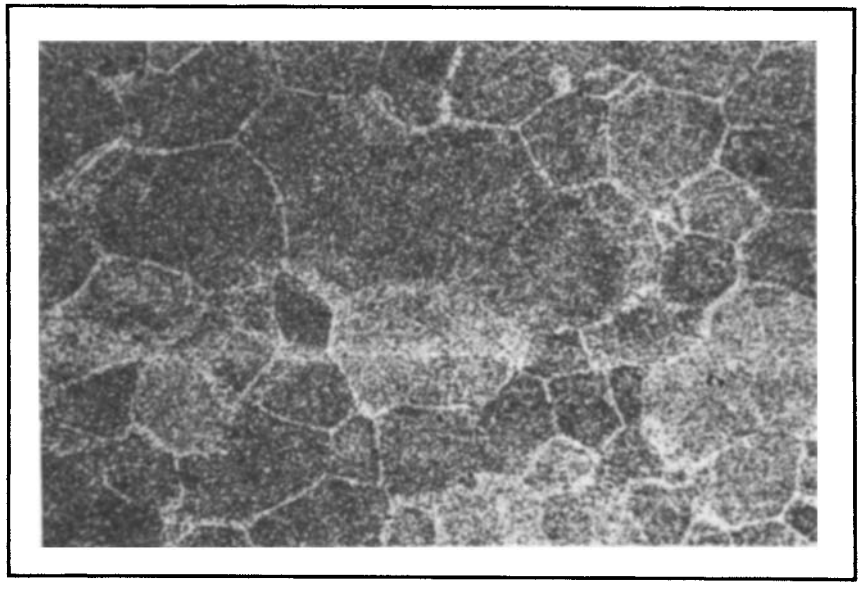

Fig. 22. 6063 extrusion in an overaged condition, showing a dense Mg_2Si matrix precipitate and a precipitate-free zone at the grain boundaries. 25% nitric acid at 70 °C (170 °F), 235×. (Courtesy of Reynolds Metals Co.)

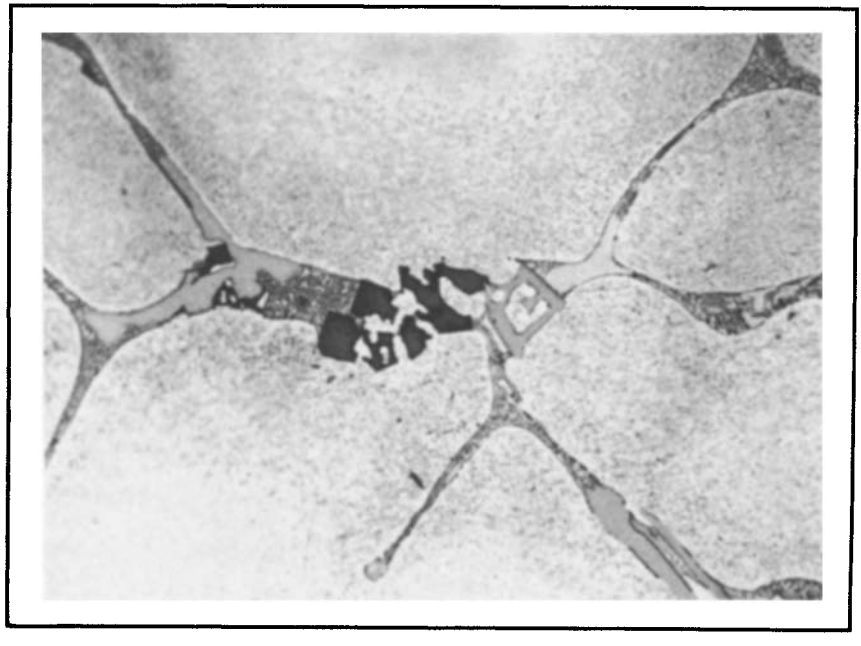

Fig. 23. 2024 as-cast ingot showing the complex multiphase structure. The fine precipitate in the aluminum matrix is formed during subsequent slow cooling of the ingot. 10% phosphoric acid, 455×. (Courtesy of Kaiser Aluminum & Chemical Corp.)

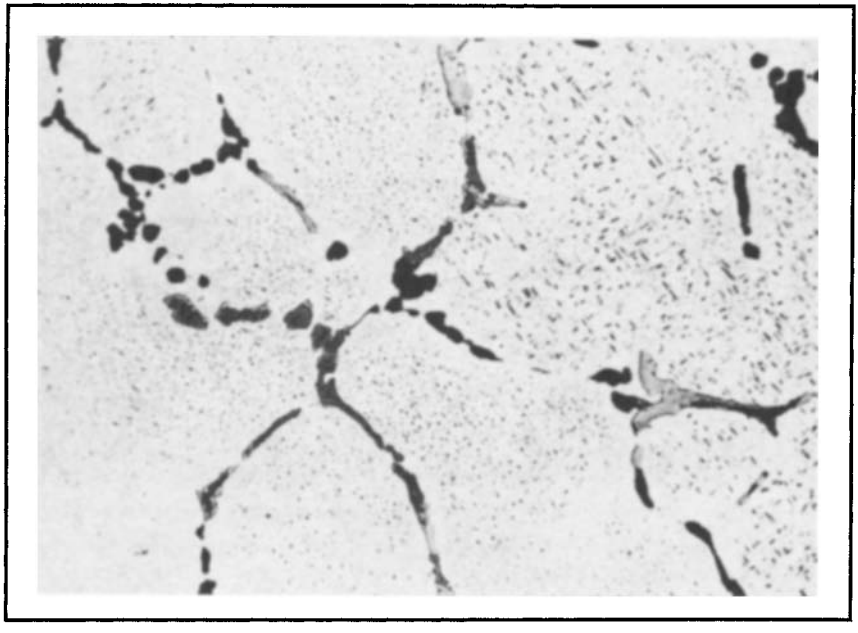

Fig. 24. 2024 heated ingot showing that the as-cast multiphase structure has been reduced to two principal iron-rich phases and soluble Al_2CuMg. The latter phase also forms Widmænstatten precipitate during subsequent slow cooling. 10% phosphoric acid, 460×. (Courtesy of Kaiser Aluminum & Chemical Corp.)

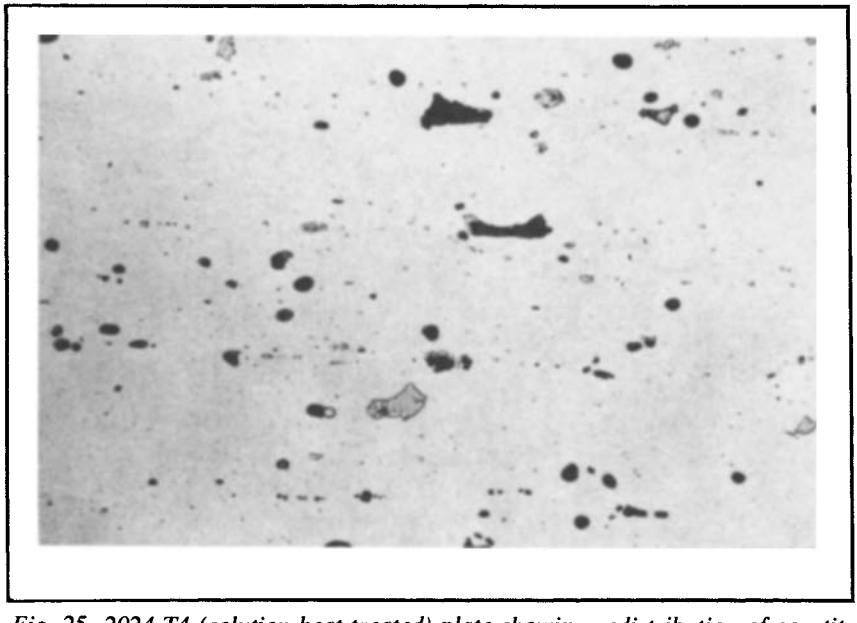

Fig. 25. 2024-T4 (solution heat treated) plate showing redistribution of constituent because of mechanical working. 10% phosphoric acid, 455×. (Courtesy of Kaiser Aluminum & Chemical Corp.)

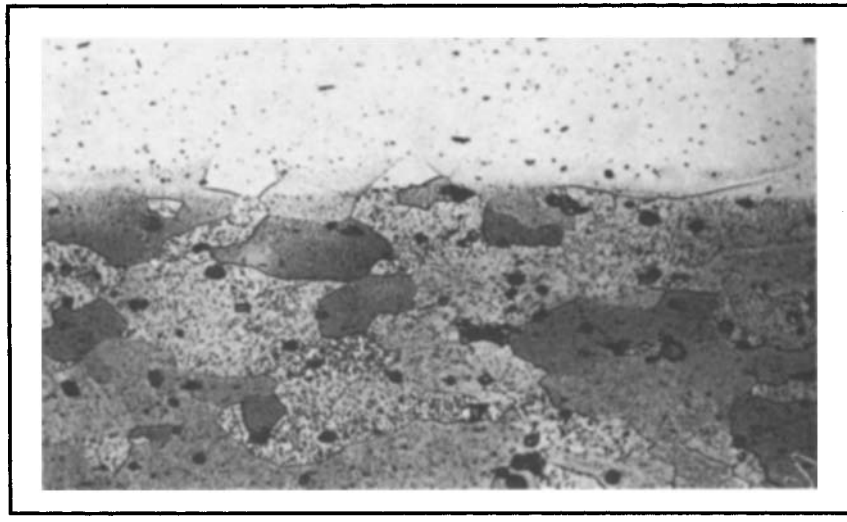

Fig. 26. Alclad 2024-T3 sheet showing some diffusion of copper into the commercial-purity aluminum cladding. Keller's etch, 460×. (Courtesy of Kaiser Aluminum & Chemical Corp.)

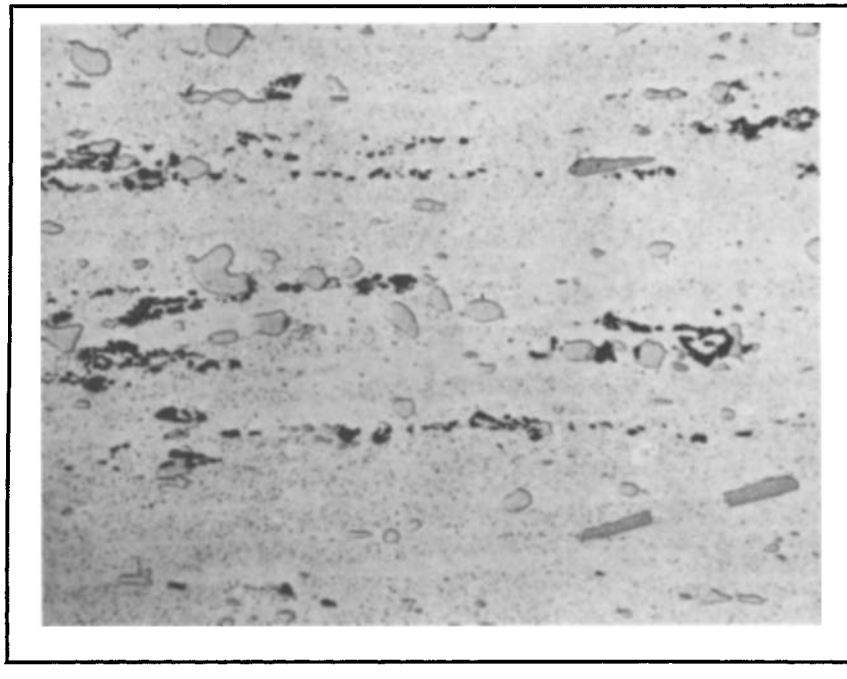

Fig. 27. 2014-F forged billet showing constituent differing from 2024. 10% phosphoric acid, 460×. (Courtesy of Kaiser Aluminum & Chemical Corp.)

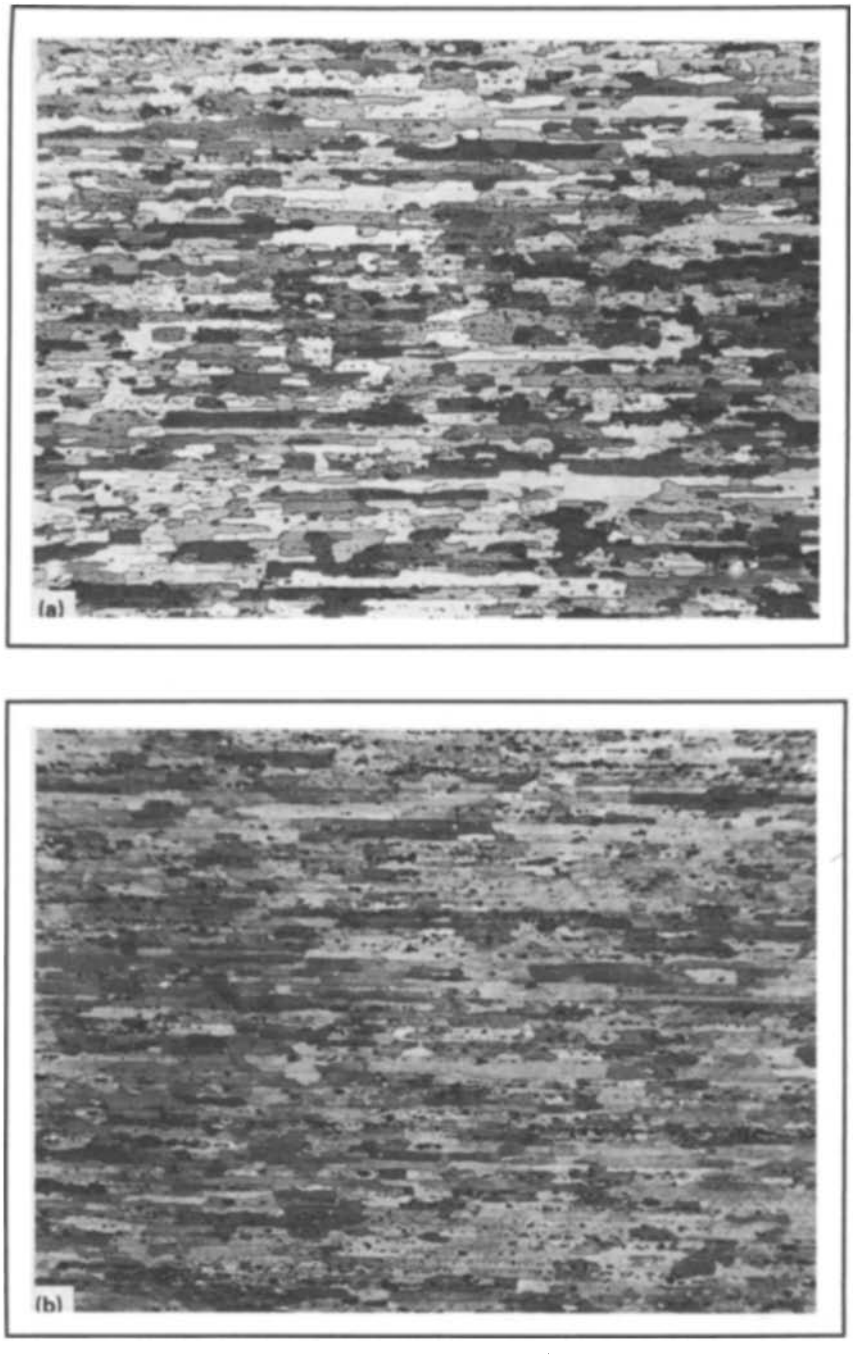

Fig. 28. 2014-T4(a) and T6(b) sheet showing reduction in etch grain contrast in the artifically aged T6 material. Keller's etch, 90×. (Courtesy of Kaiser Aluminum & Chemical Corp.)

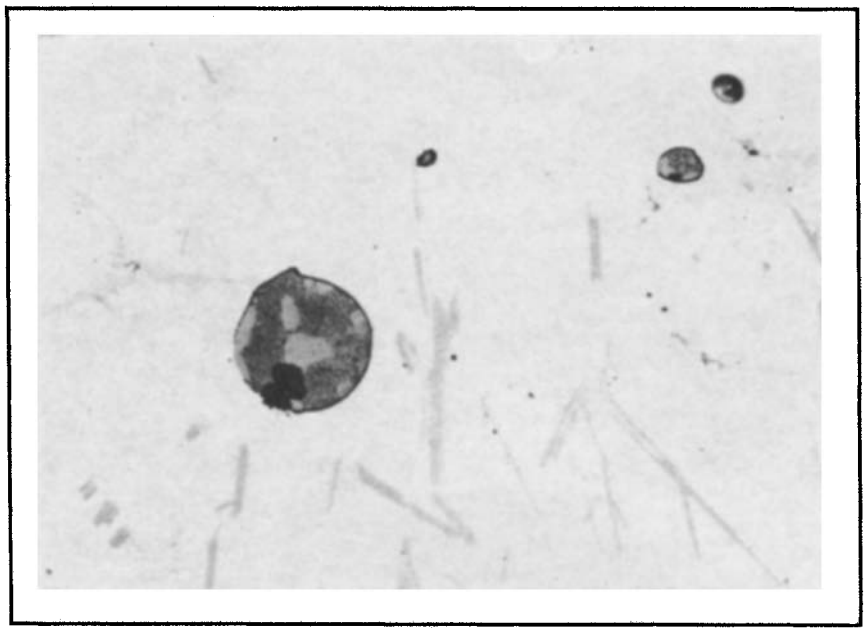

Fig. 29. 2011 as-cast ingot showing eutectic structure within the lead-bismuth globule. Unetched, 455×. (Courtesy of Kaiser Aluminum & Chemical Corp.)

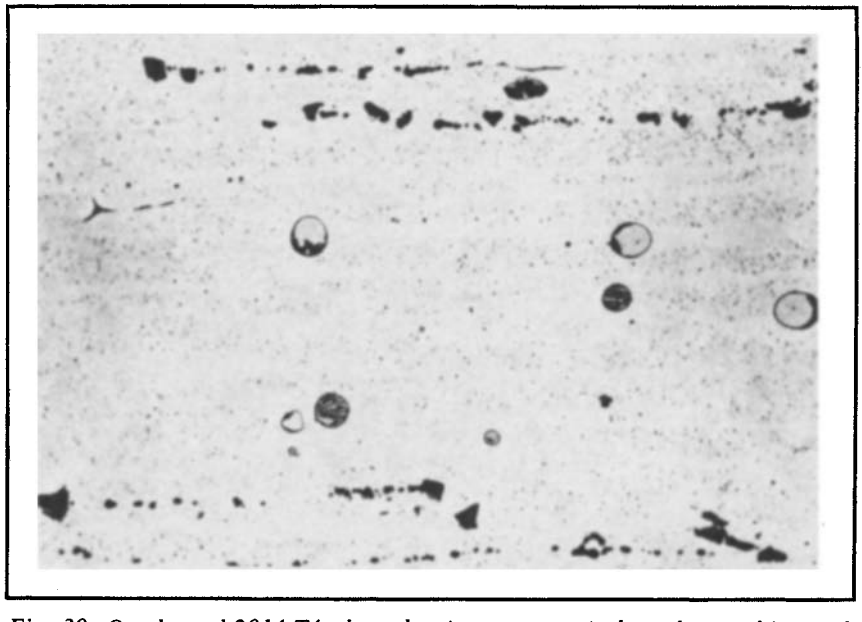

Fig. 30. Overheated 2014-T4 plate showing some grain boundary melting and formation of the liquid phase at the interface of the aluminum matrix and the $CuAl_2$ particles. Rosette structure is formed by rapid resolidification during quenching. 10% phosphoric acid, 460×. (Courtesy of Kaiser Aluminum & Chemical Corp.)

croscopic evaluation. Rosettes appear as the first stage of overheating. This is melting of undissolved eutectic (Fig. 30). Quenching while liquid is still present causes the appearance of rosettes. More extensive overheating causes grain boundary melting, particularly at triple intersections. This signals the onset of solid solution melting.

7XXX or Aluminum-Zinc Alloys. Zinc, by itself, is highly soluble in aluminum and exerts no appreciable influence on the microstructure of a simple alloy such as 7072. However, the class of alloy most frequently encountered contains magnesium and copper, as well as additives such as chromium, manganese, or zirconium, and the ever-present iron and silicon. In cast ingot form, alloy 7075 forms one or more variants of $(Fe,Cr)_3SiAl_{12}$, Mg_2Si, and a pseudobinary eutectic made up of aluminum and $MgZn_2$ (Fig. 31). The latter phase contains aluminum + copper as substitutes for zinc and can be written $Mg(Zn,Cu,Al)_2$. Subsequent heating (Fig. 32) causes the iron-rich phases to transform to Al_7Cu_2Fe. Mg_2Si is relatively insoluble and tends to spheroidize somewhat; $Mg(Zn,Cu,Al)_2$ rapidly begins to dissolve, and at the same time some Al_2CuMg precipitates, which then requires high temperatures and lengthy soaking to become completely dissolved. Chromium is precipitated from supersaturated solution as $Cr_2Mg_3Al_{18}$ dispersoid, concentrated heavily in the primary dendrite regions (Fig. 33). A well-solutionized wrought alloy contains only Al_7Cu_2Fe, $(Fe,Cr)_3SiAl_{12}$, and Mg_2Si, along with the dispersoid. Recrystallized grains are extremely elongated or flattened because of dispersoid banding, and unrecrystallized regions are not unusual even in sheet (Fig. 34). The unrecrystallized regions are made up of very fine subgrains in which boundaries are decorated by hardening precipitate. This is more obvious in hot worked structures (Fig. 35), especially in the more highly worked regions near the surface, where critical deformation has caused coarse recrystallized grains to form (Chapter 4 in this Volume). The dispersoids inhibit recrystallization and foster formation of the fine subgrain structures. $ZrAl_3$ is coherent with the matrix, and it has similar effects.

Annealing in the heat treatable alloys has a two-fold purpose: (1) the removal of residual equivalent cold work, and (2) the precipitation of solute from solid solution. The latter is accomplished by a controlled slow cooling (Chapter 5 in this Volume) and results in a random distribution of precipitate (Fig. 36). The presence of this dense precipitation makes the grain structure of such O-temper (Ref 2) alloys difficult to reveal.

Other high- and moderate-strength 7XXX alloys represent variants from 7075. Alloy 7050, with higher copper and zinc, has more Al_2CuMg to be dissolved at the solutionizing temperature. More dilute alloys can readily dissolve all of the zinc-rich phases. Signs of overheating in 7XXX alloys are usually related to segregated regions with unusual concentrations of Al_2CuMg. The homogeneous alloy has an equilibrium solidus that is well above the solution heat treating temperature range. If Al_2CuMg is present, however, very rapid heating rates can result in the appearance of rosettes, because of the inadequate time for diffusion and particle dissolution before exceeding the nonequilibrium eutectic temperature.

A given alloy cannot be characterized by a single microstructural aspect. The initial size of second-phase particles formed during solidification depends on the rate of heat removal. The degree of comminution

Fig. 31. 7075 as-cast ingot showing the multiphase structure. The fine precipitate in the aluminum matrix is formed during slow cooling from the initial ingot solidification. Dilute Keller's etch, 445×. (Courtesy of Kaiser Aluminum & Chemical Corp.)

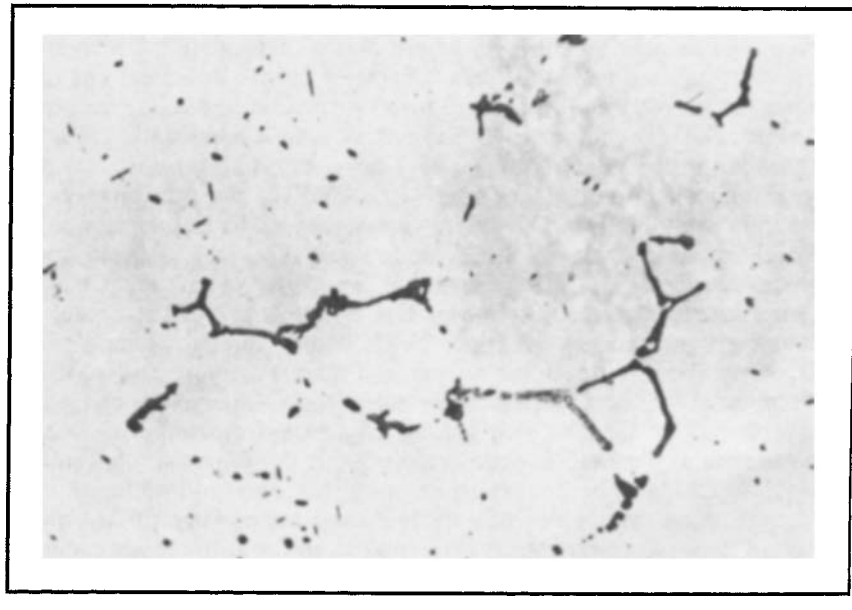

Fig. 32. 7075 homogenized ingot showing iron-rich phases, nearly insoluble Mg_2Si and soluble Al_2CuMg formed by transformation from $Mg(Zn,Al,Cu)_2$ as the latter enters solid solution. Dilute Keller's etch, 445×. (Courtesy of Kaiser Aluminum & Chemical Corp.)

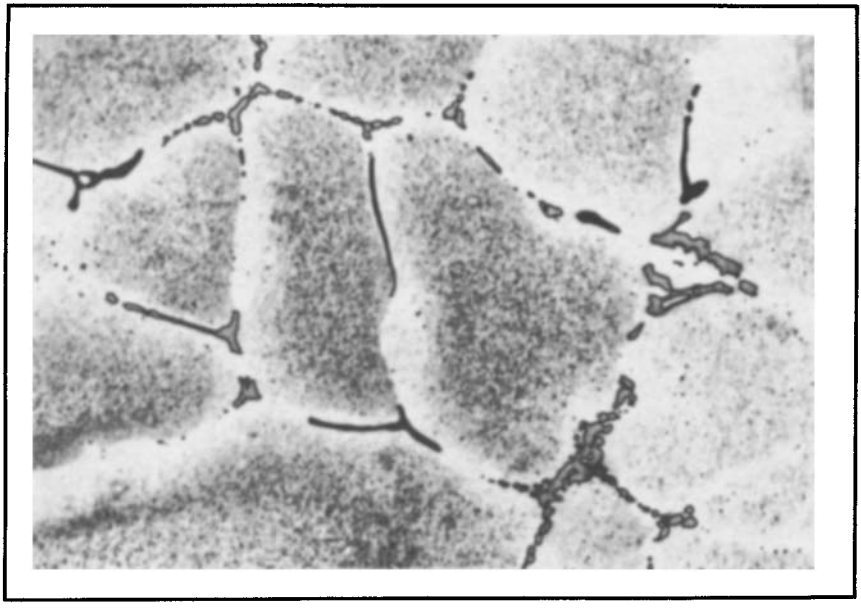

Fig. 33. 7075 heated ingot etched to reveal the fine dispersoid of the chromium-rich phase that precipitated at elevated temperatures and reflects the original distribution of chromium in the as-cast supersaturated solid solution. 0.5% hydrofluoric acid, 460×. (Courtesy of Kaiser Aluminum & Chemical Corp.)

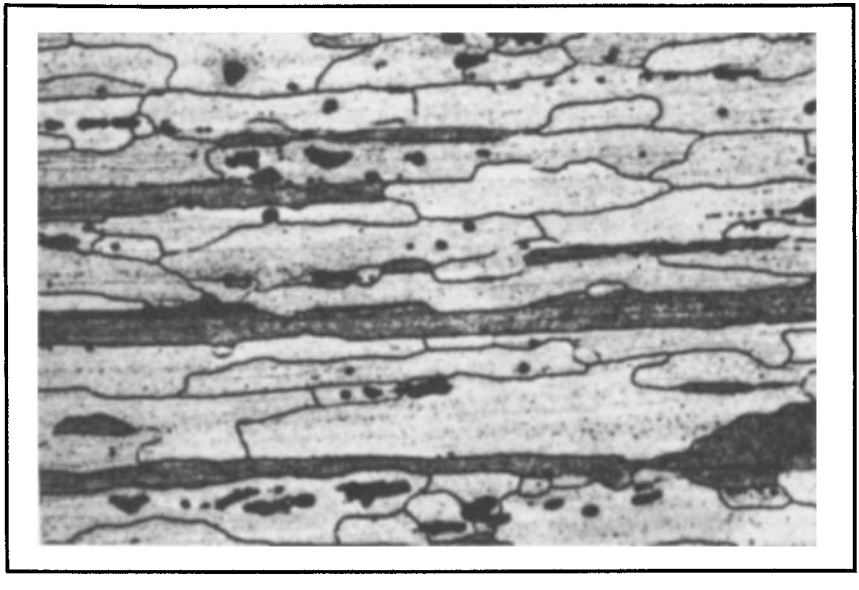

Fig. 34. 7075-T6 sheet etched to distinguish between recrystallized grains (clear) and unrecrystallized grain fragments that appear dark as a result of precipitation at boundaries of fine subgrains. 10% phosphoric acid, 455×. (Courtesy of Kaiser Aluminum & Chemical Corp.)

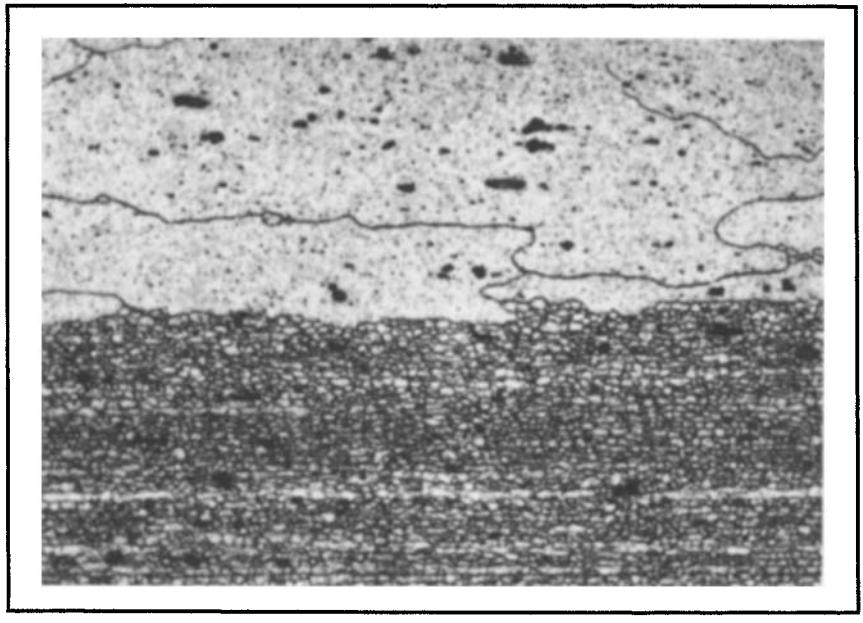

Fig. 35. 7075-T6 large extrusion with the section near the surface showing a layer of coarse recrystallized grains overlying fine subgrain structure that reflects recovery during or subsequent to hot working. 10% phosphoric acid, 455× (Courtesy of Kaiser Aluminum & Chemical Corp.)

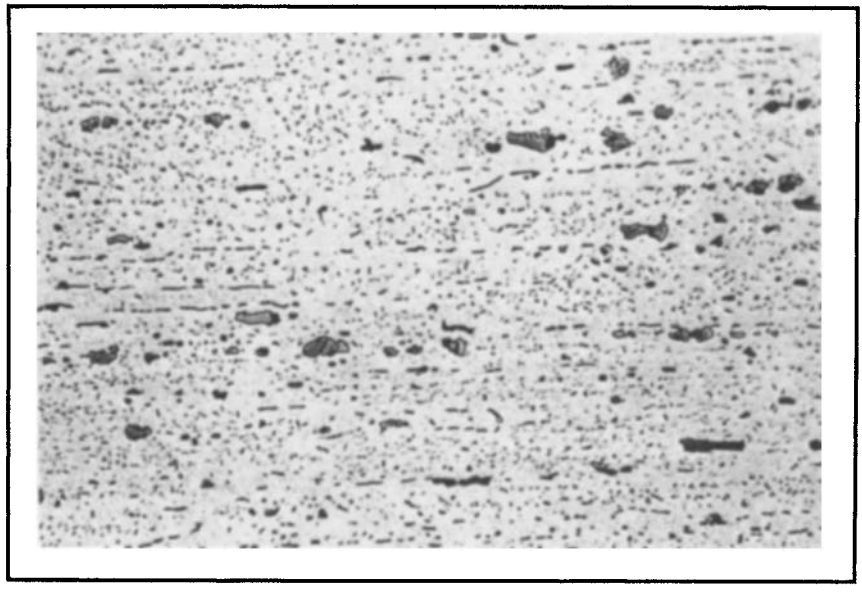

Fig. 36. 7075-O annealed sheet showing the random distribution of insoluble phases interspersed with precipitate particles of $Mg(Zn,Al,Cu)_2$ that precipitate from solid solution during controlled slow cooling from annealing. Dilute Keller's etch, 445×. (Courtesy of Kaiser Aluminum & Chemical Corp.)

and randomization of less soluble second-phase particles depends upon the total accumulation of mechanical working. The amount of excess soluble phase depends on the individual alloy composition, within specification limits, and upon the thermal treatment. The quantity and size of the dispersoid depends on the individual composition and the total thermal history, supplemented by severity of mechanical deformation. The degree of recovery and recrystallization and the size and shape of recrystallized grains depend in large measure on all of the above, as well as on factors such as rate of heating. An understanding of these interactions is important for correct interpretation of microstructural features.

QUANTITATIVE METALLOGRAPHY

The use of quantitative metallography to relate properties to microstructure is used more widely because of the introduction of automated devices. Reference 7 provides a review of techniques and theory in this field.

Microstructural features that are relevant include: (1) porosity, (2) inclusions, (3) constituent particles (insoluble phase formed during solidification, e.g., Al_6 (FeMn) or $FeAl_3$), (4) dispersoids (fine precipitate that forms during high-temperature thermal operations, e.g., $ZrAl_3$, $Al_{12}(FeMn)_3Si$, and $Al_{12}Mg_2Cr$), and (5) fine age hardening precipitates (fine, usually coherent precipitates that form at low temperature, generally as a consequence of high solute supersaturation resulting from a solution heat treatment and quench, e.g., $MgZn_2$, $CuAl_2$ (θ'), and GP zones). All of the above-mentioned features can influence the behavior of a material, and most are amenable to quantitative description.

Constituent particles, porosity, and inclusions are generally large enough to be measured optically. Features of this scale have strong effects on the fracture behavior of aluminum, especially fracture toughness, fatigue, and elongation. Constituent particles are large enough to be analyzed chemically using EMPA or scanning electron microscopy—energy dispersive x-ray (SEM-EDX) methods (for example, LeMont analysis) and hence, in multiconstituent alloys these constituents are differentiable chemically. Vruggink (Ref 8) used this approach to correlate short transverse elongations in 2×24 alloys with type and volume percent of constituent. Blau (Ref 9), Thompson (Ref 10), and Hahn and Rosenfeld (Ref 11) analyzed constituent size, spacing, and volume fraction and correlated these measurements with the fracture toughness of high-strength aircraft alloys.

Features of finer scale than the constituent (the dispersoid) are not generally measurable optically and must be measured using higher resolution techniques (TEM or SEM). These particles affect the recrystallization behavior of aluminum alloys and also can either directly or indirectly affect tensile properties. The high magnifications required and the consequent small areas that are analyzed make this random sampling difficult. If these particles are analyzed by EDX-equipped STEM, they can also be classified chemically. Features of the finest scale, the age hardening precipitates, can only be analyzed by TEM. Their effect is primarily to increase yield and tensile strength.

Staley (Ref 12) related fatigue behavior of aluminum high-strength 7x75 alloys to constituent content. At high levels of stress intensity, the growth

rates of fatigue cracks were lower for a lower constitutent alloy (7475) than for the higher constituent content of 7075. At low-stress intensity, constituent particles may beneficially pin dislocations.

SCANNING ELECTRON MICROSCOPY (SEM)

A good description of how SEM works and some of its applications to fracture surface studies can be found in *Practical Scanning Electron Microscopy* by Goldstein *et al* (Ref 13). The chief advantages of SEM analysis are:

- Easy specimen preparation
- Widest range of magnification available (commonly from 15 to 50,000 diameters)
- Ability to observe large areas of specimen surface, including origin and propagation zones, because 645 mm^2 (1 $in.^2$) or more of the fracture surface can be directly placed into the microscope
- Excellent depth of field for focusing on surfaces with large topography variation
- Ability to view the fracture face and simultaneously perform microchemical analysis if the microscope is so equipped

Disadvantages of SEM analysis have related to uncertain specimen tilt or orientation in the microscope that can alter the apparent size of fracture features, such as fatigue striation spacings, or influence quantitative microchemical analysis (actual takeoff angle of x-ray from specimen surface). The use of stereo pair SEM images offsets this disadvantage, for they can precisely define surface topography. In addition, uncertain fracture surface topographies may be encountered because of the lack of well-documented literature of SEM fracture surfaces.

Scanning electron microscopy micrographs of fracture surfaces are performed by two types of emitted electrons. Secondary electrons are most commonly used because of their fidelity in showing topographical features. Higher energy, back-scattered electrons can be used to show average compositional variations across a fracture surface, usually with only a slight degradation of surface detail. Actual microchemical identification of the elements on a fracture surface usually involves examination of the characteristic x-rays emitted from the surface because of ionization processes caused by an incident electron beam. Characteristic x-rays fingerprint the identity of elements present and are detected by either a solid-state detector that is sensitive to the x-ray energy, or by a wavelength dispersive detector that is sensitive to the x-ray wavelength.

Examples of SEM imaging and microchemical analysis, contrasted against TEM imaging of replicas, follow. Figure 37 is an SEM secondary electron image clearly showing fatigue cracking in 2024 aluminum. Note the resulting great depth of field, despite large topographic differences. Measurements of fatigue striation spacing cannot generally be made without detailed knowledge of local specimen surface tilt relative to the electron beam and secondary electron detector or by the use of stereo pairs. Figure 38 is a TEM image of a replica of the same fatigue fracture. Here, striations are clearly visible and can be measured to determine fatigue crack growth rate. However, a pitfall similar to that of SEM is encoun-

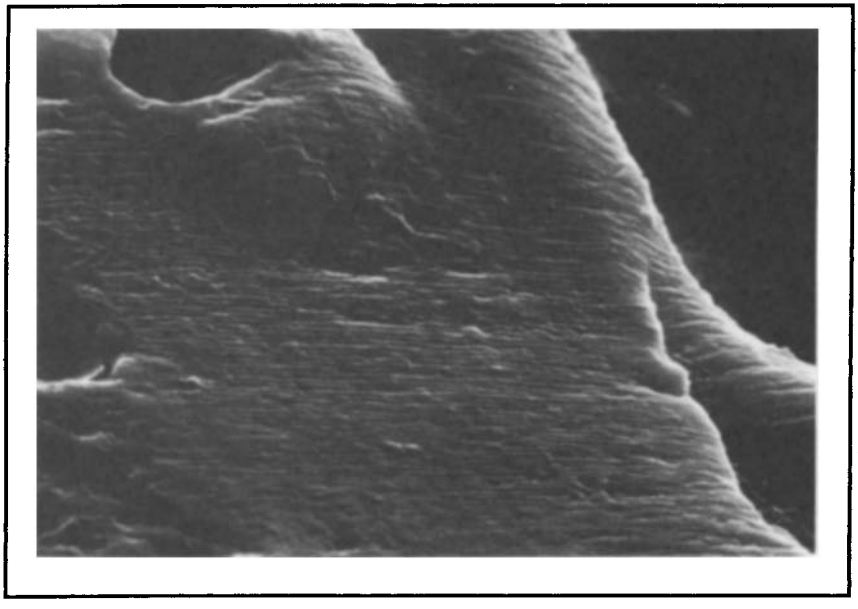

Fig. 37. SEM secondary electron image showing fatigue fracture in 2024 aluminum (4600×). (Courtesy of Boeing Commercial Airplane Co.)

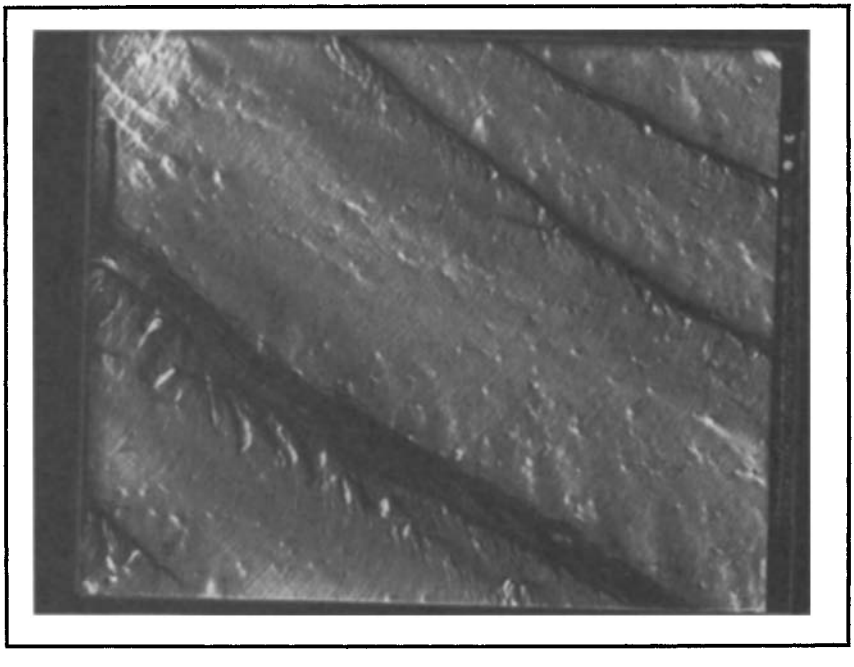

Fig. 38. TEM replica showing fatigue fracture in 2024 aluminum (4075×). (Courtesy of Boeing Commercial Airplane Co.)

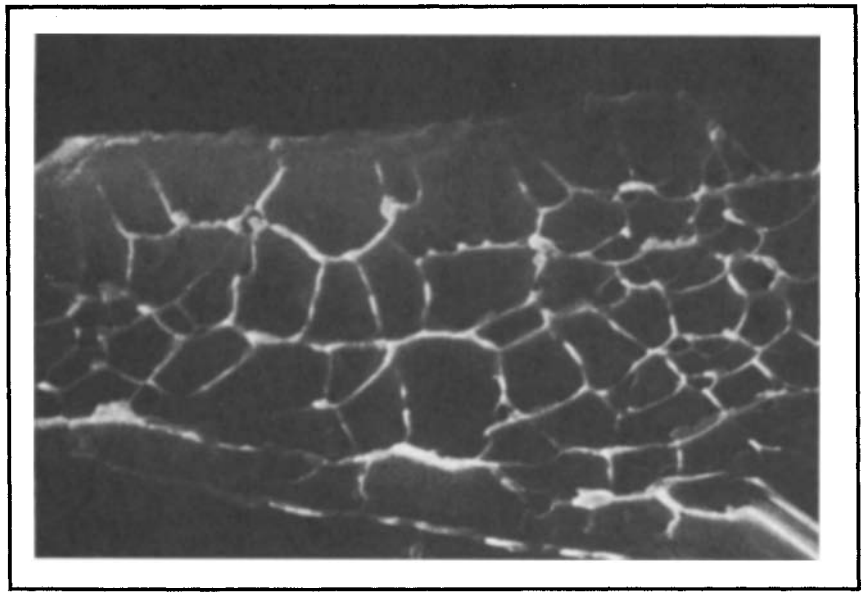

Fig. 39. SEM imaging of tensile fracture in A357 casting (18,400×). (Courtesy of Boeing Commercial Airplane Co.)

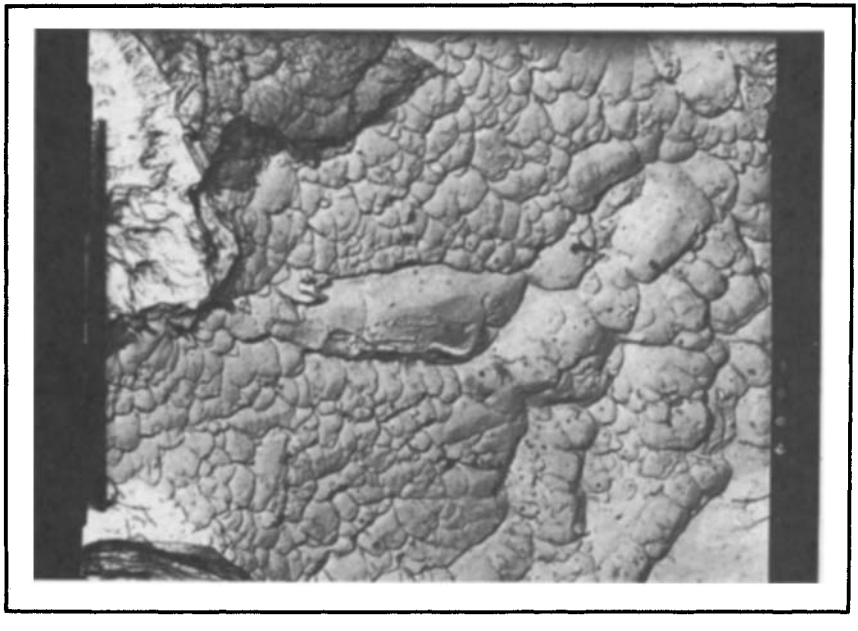

Fig. 40. TEM replica imaging of tensile fracture in A357 casting (6550×). (Courtesy of Boeing Commercial Airplane Co.)

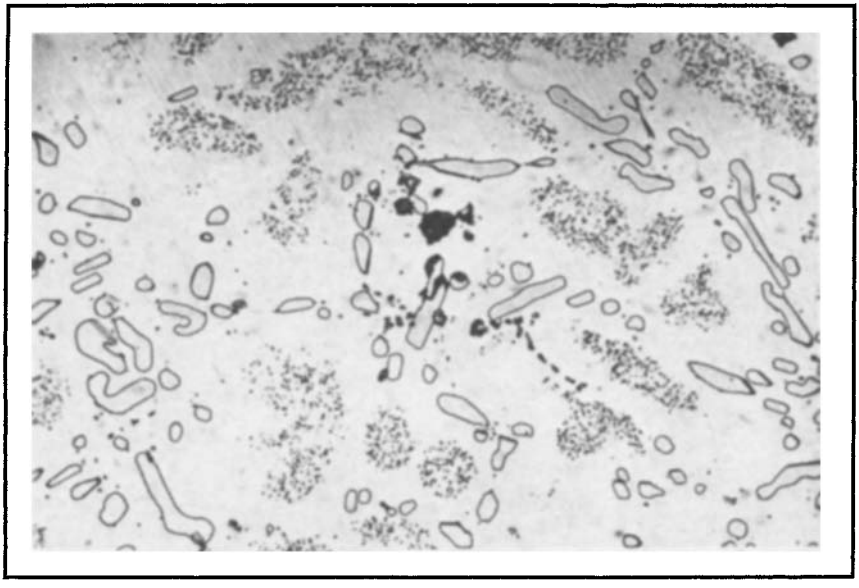

Fig. 41. Light optical image of a polished section of A357 casting (380×). (Courtesy of Boeing Commercial Airplane Co.)

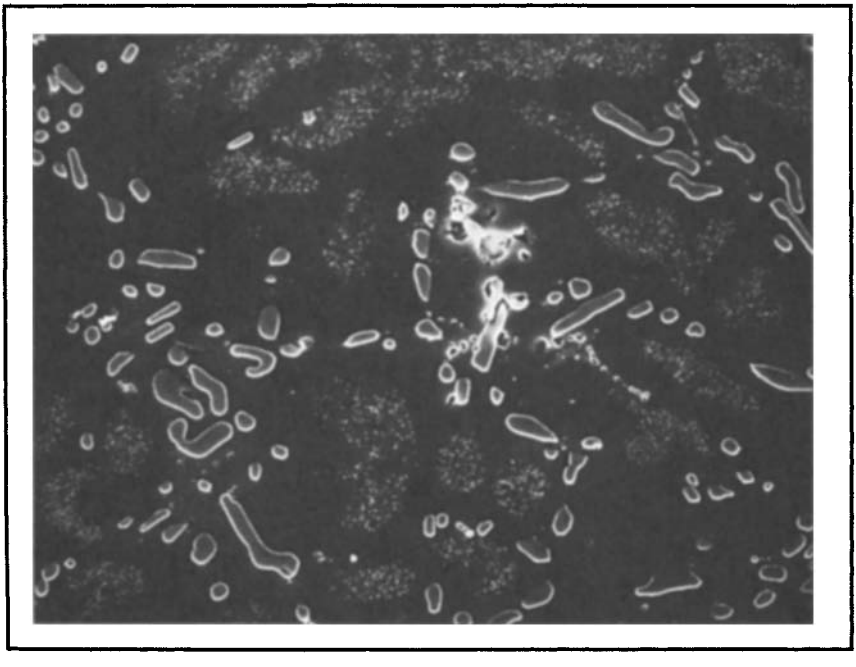

Fig. 42. SEM imaging of a polished section of A357 casting (385×). (Courtesy of Boeing Commercial Airplane Co.)

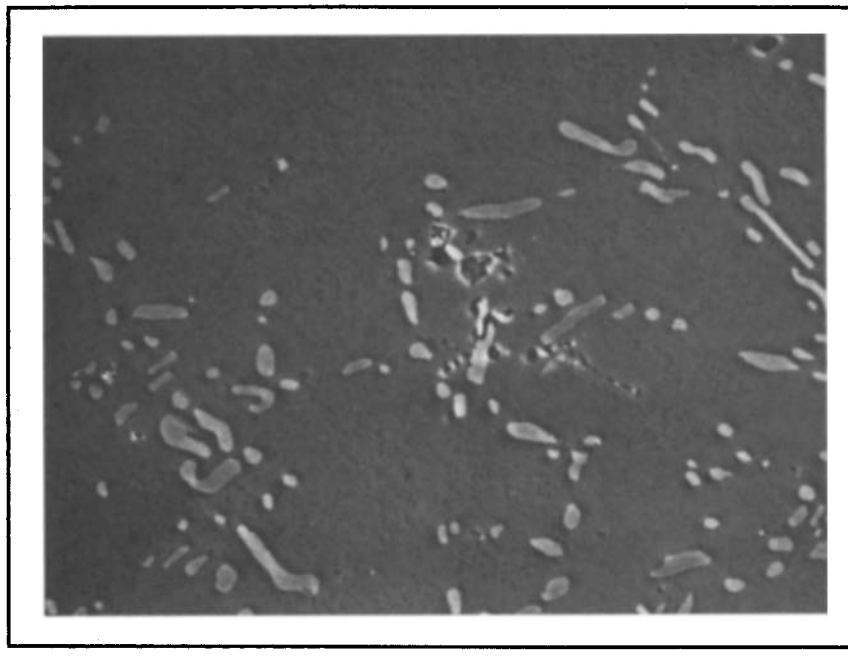

Fig. 43. Back-scattered electron imaging of a polished section of A357 casting (385×). (Courtesy of Boeing Commercial Airplane Co.)

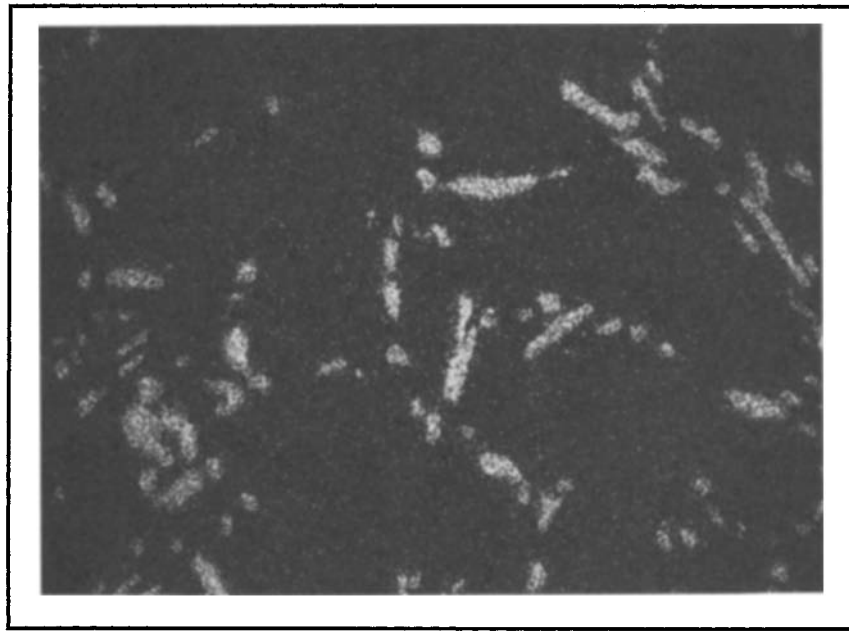

Fig. 44. Silicon x-ray map of a polished section of A357 casting (385×). (Courtesy of Boeing Commercial Airplane Co.)

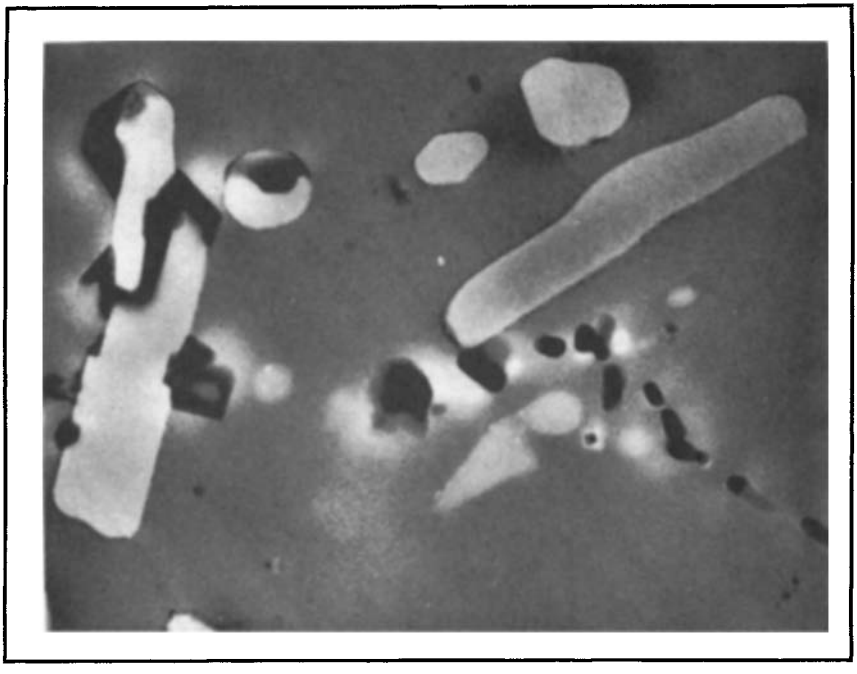

Fig. 45. Back-scattered electron imaging of a polished section of A357 casting (2300×). (Courtesy of Boeing Commercial Airplane Co.)

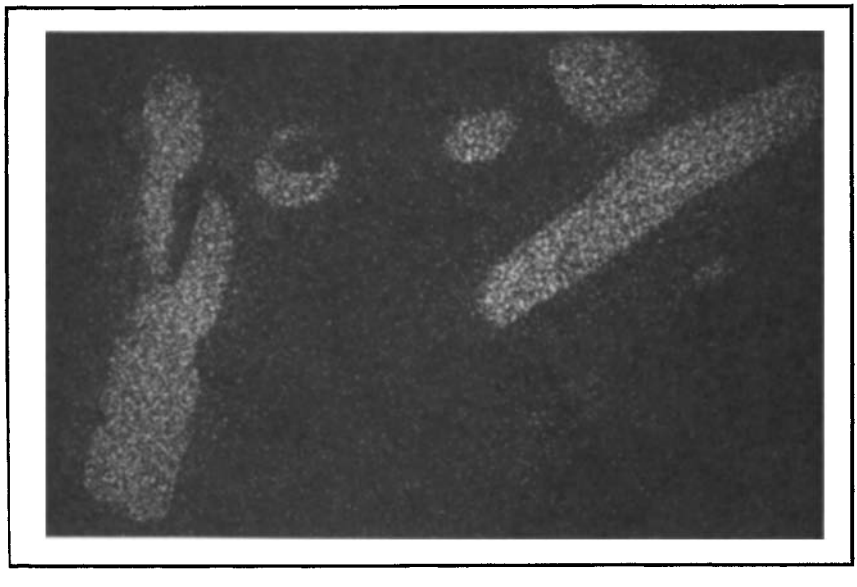

Fig. 46. Silicon x-ray map of a polished section of A357 casting (2300×). (Courtesy of Boeing Commercial Airplane Co.)

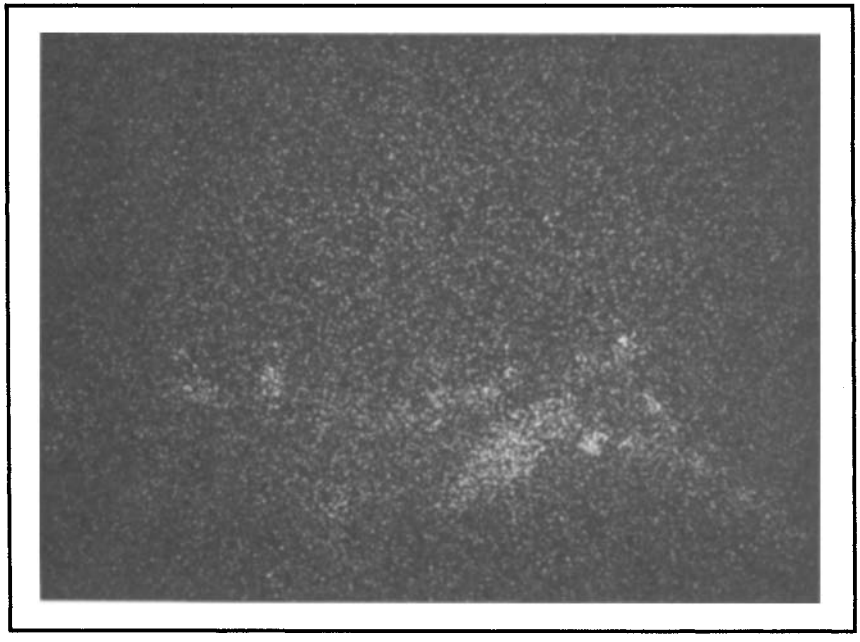

Fig. 47. Iron x-ray map of a polished section of A357 casting (2300×). (Courtesy of Boeing Commercial Airplane Co.)

tered. The striation spacing observed must be representative of the principal crack front. This is not always clear, because the act of replicating fracture surfaces presents the probability that despite their planar appearance, the striations observed can derive from local out-of-plane crack front geometry.

Dimple topography characteristic of microvoid coalescence in tensile and shear mode fractures is exhibited by SEM and TEM imaging in Fig. 39 and 40, respectively, for A357 casting alloy. An example of the microchemical analysis advantage afforded by SEM is demonstrated on a polished section of A357 as shown in Fig. 41 through 47. Figures 41 and 42 are light optical and SEM secondary electron images, respectively, showing identical fields of view. Phases dissolved by the etchant are clearly shown as holes in the SEM image. When imaged using back-scattered electrons, as in Fig. 43, this same field contains small patches of micropitting, appearing as white in color by secondary electron imaging, and black in color by light optical methods. The use of back-scattered electron imaging permits qualitative knowledge of the relative average atomic number of differing phases; silicon-containing particles (see x-ray map in Fig. 44) absorb fewer electrons, and silicon has a higher back-scattered coefficient than the aluminum matrix and appears light in Fig. 43. A detailed examination of the center region of Fig. 41 through 43 shows the presence of both silicon-rich and iron-rich phases (Fig. 45 through 47) by back-scattered electron imaging.

Intergranular primary and secondary cracking in 7075 alloy are shown in Fig. 48 and 49, SEM and TEM images, respectively. Corroded areas

on this fracture face, including elements of the corrosion product, are shown by SEM secondary electron and TEM imaging, Fig. 50 and 51, respectively. The light rectangle of Fig. 50 defines a region of SEM-EDX analysis, which showed the corrosion product to contain sodium and chlorine, in addition to alloying elements. Both SEM and TEM imaging of fracture faces are generally far superior to light optical methods. The specific advantages of SEM techniques, allowing microchemical analysis *in situ,* as well as superior imaging, continues to become more important as the number and scope of documented fracture topographies grows.

TRANSMISSION ELECTRON MICROSCOPY (TEM)

Developments in instrumentation and techniques during recent years have enabled electron microscopy to play an increasingly important role in advancing the understanding of aluminum alloy microstructure. The high magnification, resolving power, and excellent depth of focus enable the ultrafine details of the microstructure to be imaged in these instruments. When ultrafine detail is needed, TEM methods are preferable to optical microscopy. Magnifications of up to 300,000× and resolutions better than 0.5 nm (5 Å) are routinely available.

Transmission electron microscopy is usually carried out using thin foil specimens that have been carefully prepared from the sample of interest, although for some investigations, replicas of the specimen surface can be used. In standard 100-kV TEM, aluminum alloy specimens must be prepared so that the area of interest is less than about 0.5 μm (0.02 mil) thick and preferably as thin as 0.2 μm (0.008 mil). Elaborate techniques including jet electropolishing and ion beam erosion have been developed to prepare such specimens. The contrast in electron microscope images arises as the result of differences in the diffraction and absorption of the electrons by different features in the specimen.

Localized changes in orientation that occur at grain and subgrain boundaries and in the strain fields associated with dislocations and coherent precipitates cause contrast variations. Similarly, the different crystal structure factors and absorption coefficients of second-phase particles also produce image contrast. Although the specimens are thin, the image is a projection of a three-dimensional structure, and the orientation and distribution of features can be established three-dimensionally.

In addition to excellent imaging capabilities, TEM can also be used for electron diffraction. In this mode of operation, areas of the image as small as 1 μm (0.04 mil) can be selected, and diffraction patterns can be obtained. These selected area diffraction patterns are used extensively to identify second-phase particles and to establish crystallographic orientations of an area or particle of interest.

Scanning transmission electron microscopy (STEM) offers an even more impressive range of capabilities. In these instruments, the incident electron beam is demagnified to produce a very small spot size, typically between 0.1 and 50 nm (1 and 500 Å) at the specimen, and this is scanned in a raster over the area of interest. With appropriate detectors, a number of different imaging modes can be selected. Thus, in addition to the scanning transmission image (similar to TEM), secondary electron images

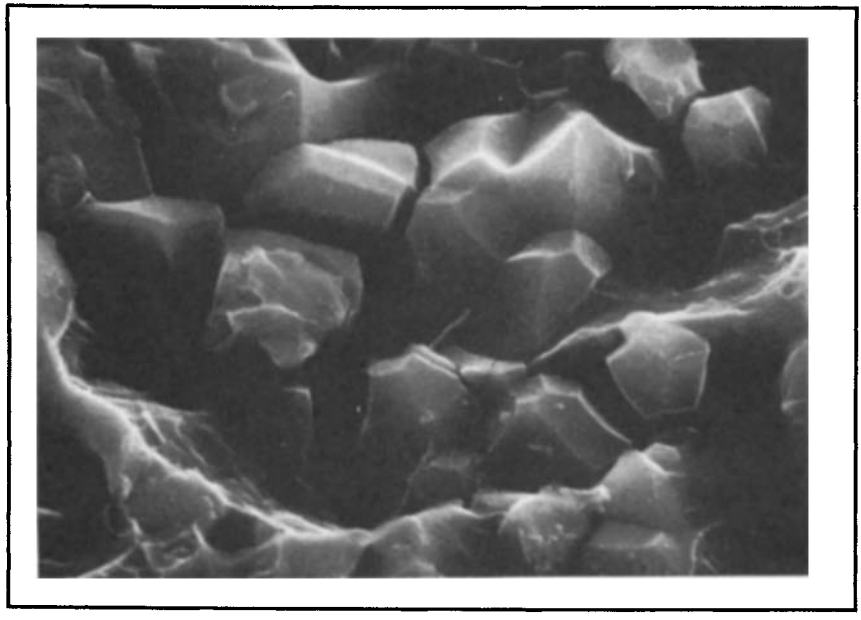

Fig. 48. Intergranular stress-corrosion cracking in 7075 alloy with SEM imaging (9200×). (Courtesy of Boeing Commercial Airplane Co.)

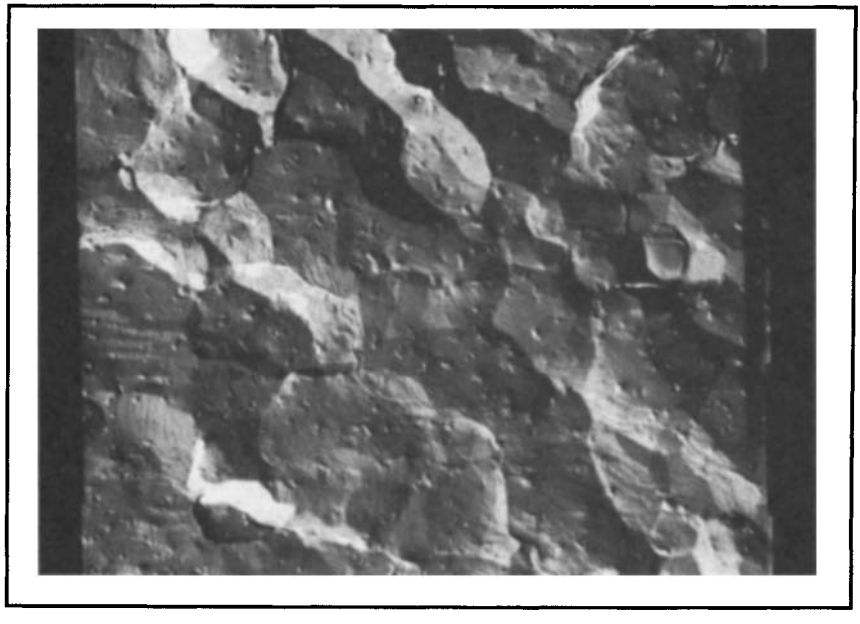

Fig. 49. Intergranular stress-corrosion cracking in 7075 alloy with TEM imaging (5830×). (Courtesy of Boeing Commercial Airplane Co.)

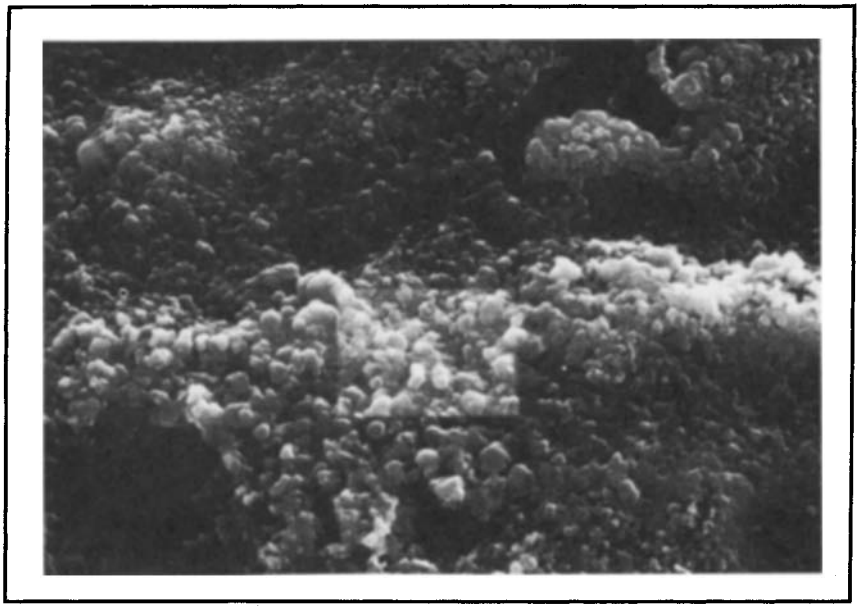

Fig. 50. Stress-corrosion product of 7075 alloy with SEM imaging (4325×). (Courtesy of Boeing Commercial Airplane Co.)

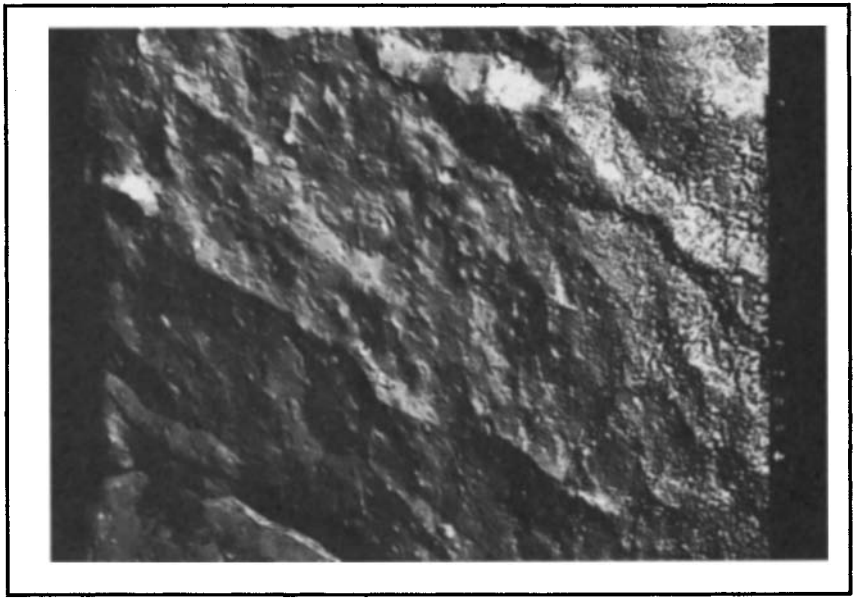

Fig. 51. Stress-corrosion cracking and product of 7075 alloy with TEM imaging (4075×). (Courtesy of Boeing Commercial Airplane Co.)

(surface), back-scattered electron images (atomic number contrast), and x-ray images (composition maps) can be selected.

In addition to excellent imaging facilities, STEM has the capability to generate and accurately position a fine electron beam on a small area of a specimen. This ability is of particular value for microdiffraction and microanalysis. Microdiffraction patterns provide crystallographic information from very small features, and by using an energy-dispersive x-ray detector, quantitative microanalysis from regions of thin specimens less than 100 nm (1000 Å) in diameter are readily obtainable in many cases.

High-voltage electron microscopy (HVEM), using instruments that operate at up to 1 million V, enable thicker specimens to be studied in transmission. This method is used for *in situ* experiments involving observations during heat treatment or straining. Expense and specialization have limited use of HVEM to a few research centers.

Even more sophisticated imaging and microanalytical techniques are being developed that offer opportunities to study aluminum microstructure in greater detail. High-resolution TEM is capable of directly imaging the lattice structure of aluminum and has contributed to the understanding of lattice defects and the early stages of zone formation in some alloy systems. The ultimate high-resolution imaging and analytical devices, however, are the field ion microscopes and atom probes that, with suitable specimens, can image and identify individual atoms. Using these instruments, investigations of segregation of alloying elements to grain boundaries or other defects may be possible in the near future.

Structural Features. Many of the structures observed by light microscopy can be studied in more detail in the electron microscope. Furthermore, a great deal of information that cannot be obtained by light microscopy is available. Thus, in addition to the familiar grain structure of the material, subgrains and dislocation substructures can be observed, and if required, crystallographic orientations can be measured using electron diffraction patterns.

Grain boundaries generally appear as bands that have widths corresponding to their magnified projections. This boundary image width is determined by the inclination of the boundary with respect to the location beam direction and the thickness of the specimen. These grain boundary images have distinct fringes running along their lengths. The fringe contrast is the result of electron diffraction effects, and the number and contrast of the fringes vary if the diffraction conditions are changed by specimen tilting.

The electron microscope can also reveal dislocation networks that are introduced during deformation processes and subsequent changes that occur during recovery and recrystallization. The lattice strain associated with a dislocation causes a change in the local diffraction conditions, causing dislocation contrast. Dislocations normally appear as lines that terminate at the specimen surface, although helices and loops can be present in certain cases. The best dislocation images are obtained by a technique known as weak beam dark field imaging. Using this method, only regions of highest lattice distortion (near the dislocation cores) appear in the image.

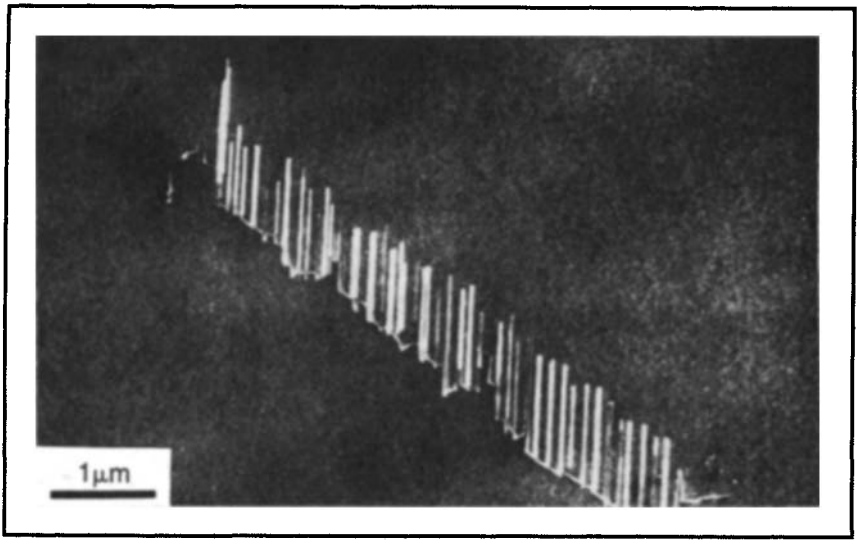

Fig. 52. Weak beam dark field imaging. β-Mg_2Si needle-like precipitates that have nucleated and grown in association with a dislocation in a sample that was solution treated and cooled directly to 270 °C (515 °F). (Courtesy of Alcan International Ltd.)

The weak beam technique is also useful for studying the strain fields associated with Guinier-Preston (GP) zones and fine coherent precipitates (Fig. 52). These zones are extremely small clusters of solute atoms in the solid-solution matrix and are the precursors of precipitate particles. Examinations of fine precipitates and dispersoids are frequently carried out using TEM. Size distributions and the spatial distribution of particles within the substructure can be obtained by standard imaging techniques. The dispersoid particles frequently occur at grain or subgrain boundaries, on dislocations, or at the interface with other particles. Some types of particles develop at apparently random sites within the matrix, although the nucleation may be associated with point defects such as vacancies.

Certain precipitate particles grow with characteristic shapes and can often be tentatively identified in this way. In cases where this is not possible or where a more positive identification is required, electron diffraction and thin foil microanalysis can be used to characterize the crystallographic structure, orientation, and composition of particles (Fig. 53). Thin foil microanalysis can also be used in some cases to determine the concentrations of elements in solid solution in the aluminum matrix. The high spatial resolution of ≤50 nm (≤500 Å) for microanalysis, which is available in a STEM system, enables the establishment of matrix compositions between dispersoid particles. Studies of concentration profiles of elements in the vicinity of grain boundaries have also been made.

Electron Microstructure of Wrought Alloys. A wide range of aluminum alloys has been studied by electron microscopy, and characteristic microstructures of the more common alloy systems after various fabrication and thermal treatments have been described. In general, plastic

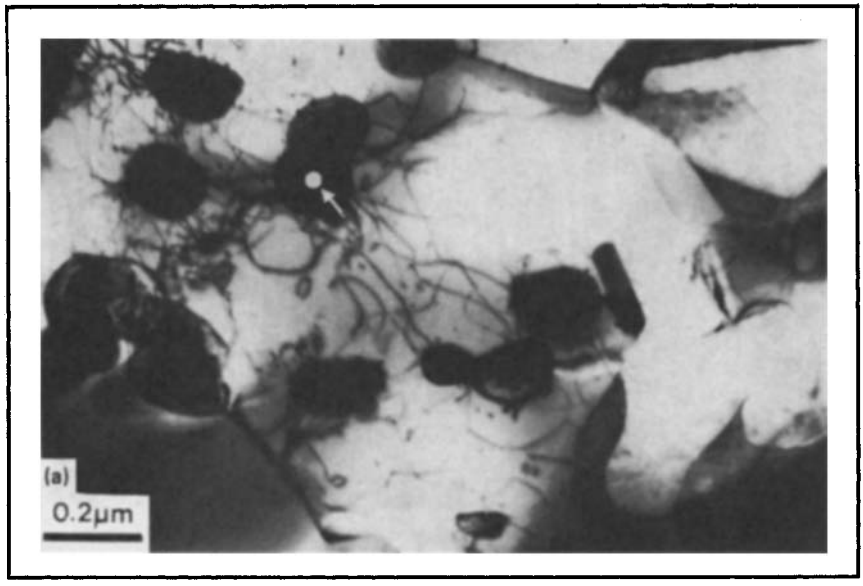

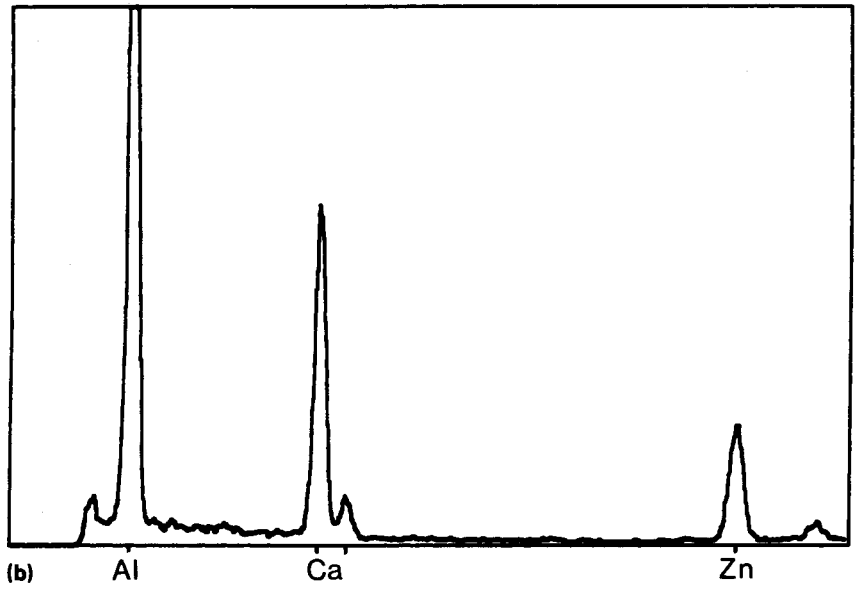

Fig. 53. (a) Energy dispersive microanalysis of a small particle in STEM. (b) The spectrum from the arrowed particle in a sample of an aluminum-calcium-zinc superplastic alloy. (Courtesy of Alcan International Ltd.)

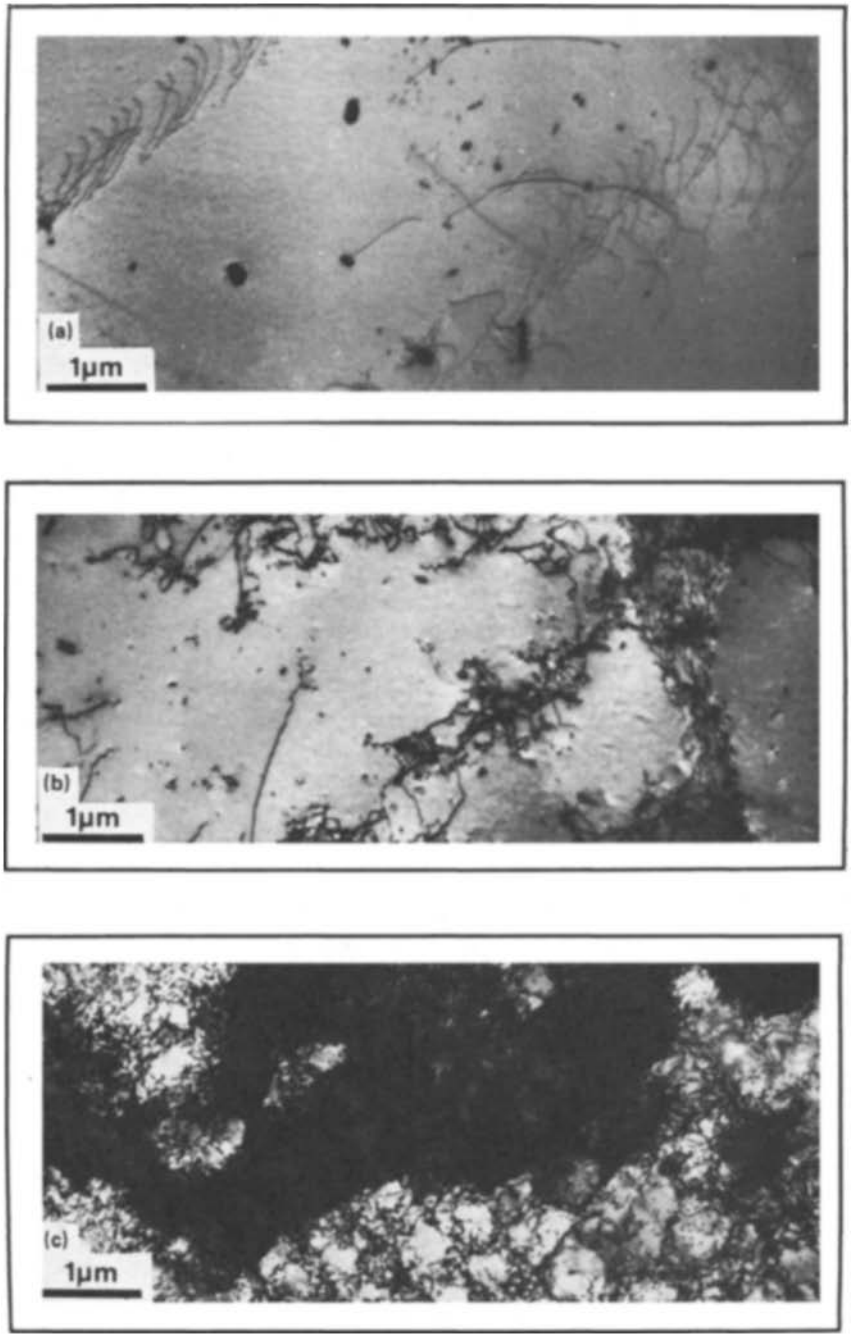

Fig. 54. A sequence of micrographs showing substructure development during cold rolling. (a) 2% reduction; isolated dislocations and slip bands. (b) 5% reduction; early stages of the development of cellular dislocation networks. (c) 60% reduction; well-developed cellular structure. (Courtesy of Alcan International Ltd.)

deformation of an aluminum alloy is usually associated with an increase in dislocation content. The nature and distribution of the resulting substructures depends on the extent, temperature, and rate of deformation, and also on other microstructural conditions such as grain size, particle size, and distribution.

In commercially pure aluminum (1XXX), a small amount of cold deformation generates a low density of essentially isolated dislocations (Fig. 54). As the deformation increases, dislocations increase in number and become concentrated in tangles along slip bands. With still further deformation, tangles increase in number and density, and a cellular network is developed, with tangles of dislocations surrounding relatively dislocation-free areas. In other alloy systems, similar changes in the dislocation substructure are observed, although they are modified by the presence of the alloying elements. Where coarse, hard particles ($\gtrsim$1 μm or $\gtrsim$0.04 mil) are present in an alloy before cold working, a high density of dislocations develops in their vicinity (Fig. 55). In alloys with a dense dispersion of finer particles ($\lesssim$0.1 μm or $\lesssim$0.004 mil), development of slip bands tends to be inhibited and a more homogeneous dislocation distribution is generated. If elements such as magnesium are present in solid solution during deformation, the dislocation mobility is reduced by interaction with the solute atoms. This results in a more rapid buildup of dislocations and is responsible for the more rapid work hardening observed in alloys such as 5182.

During the heat treatment of aluminum alloys, changes in properties create corresponding changes in microstructure. The detailed microstructural changes that occur depend on the particular alloy, its fabrication

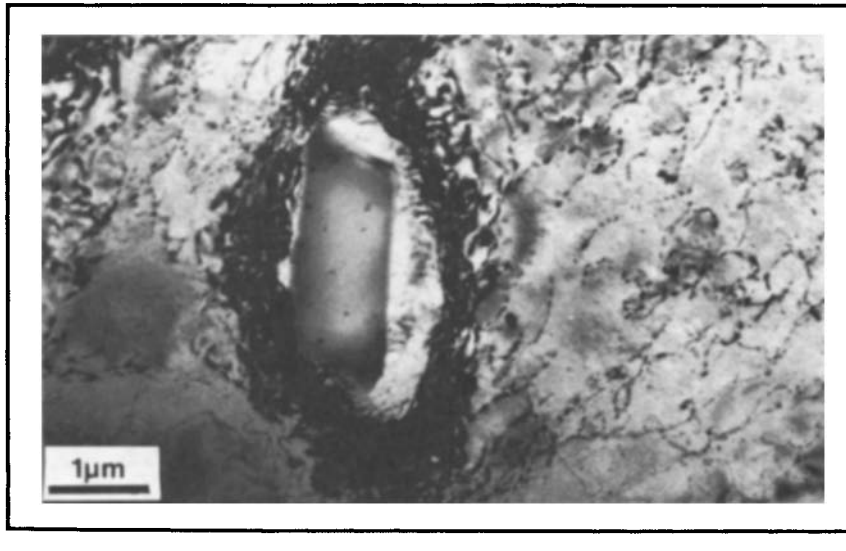

Fig. 55. Region of high local deformation in the vicinity of a coarse $FeAl_3$ particle in a cold rolled sample (20% reduction). (Courtesy of Alcan International Ltd.)

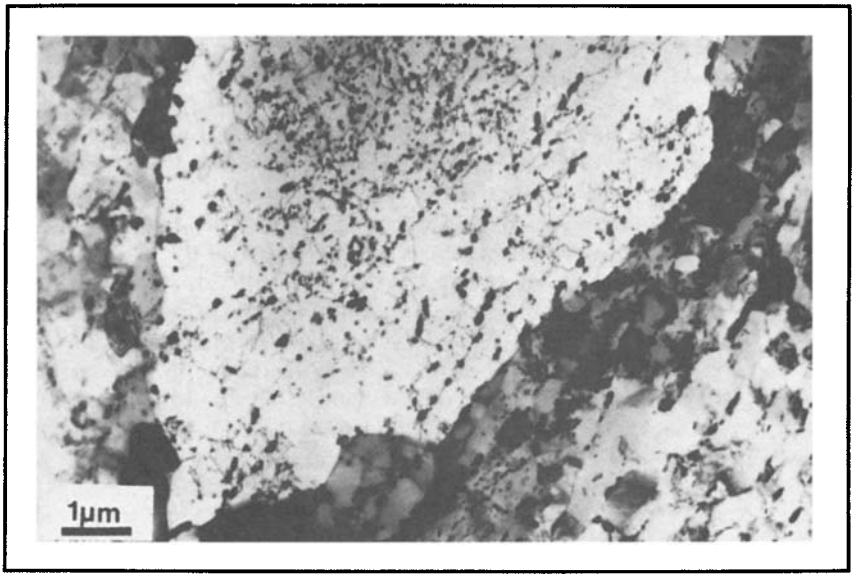

Fig. 56. An early stage of recrystallization of AA3003, showing a new grain growing into the substructure. The manganese-bearing precipitates interact strongly with the moving boundary and retard its progress. (Courtesy of Alcan International Ltd.)

history, and the temperature and duration of heat treatment. Commercial heat treatments can produce a number of microstructural changes including particle dissolution, particle coarsening, precipitation, changes in dislocation distribution and density, and the development and migration of subgrain and grain boundaries. In many cases, several of these phenomena occur simultaneously and often interact so that, for example, a precipitation process may significantly inhibit subgrain boundary migration.

In a number of alloy systems, the most important microstructural changes that occur involve changes in the dislocation and subgrain structures. As an example of the sort of change that can occur in this type of alloy, heat treatment of cold rolled (1XXX) alloy can be considered. At low temperatures ($\lesssim$100 °C or $\lesssim$212 °F), changes in dislocation density that occur are insignificant. At higher temperatures, dislocations become more mobile, rearranging themselves into lower energy configurations, and decrease in density by mutual annihilation or escape. As this recovery process proceeds, cellular dislocation tangles develop into subgrains with well-defined, low-misorientation boundaries. If the heat treatment temperature is sufficiently high, discontinuous recrystallization occurs, and new grains nucleate at favorable sites and grow rapidly to consume the dislocation and subgrain structures.

The recovery and recrystallization phenomena described here can occur in most aluminum alloys under the appropriate conditions. However, the kinetics and temperatures at which the microstructural changes are observed vary depending on the particular alloy and its condition. The sizes

and distribution of particles and the presence of elements in solid solution can significantly modify behavior during annealing.

A number of commercial alloys are supplied in the fully recrystallized condition (O temper) to be used in forming applications (1XXX, 3XXX, and 5XXX). For many applications of these alloys, a fine grain size is desirable, because a coarse-grained material causes surface roughening during forming (orange peel effect). Achieving a fine grain size often requires rigorous compositional and processing control. The number of potential recrystallization nuclei can often be related to the size and distribution of coarser particles in the alloy and can therefore be modified to some extent by homogenization. The growth of these potential nuclei into new grains is markedly affected by the size and distribution of finer dispersoid particles and, to a lesser extent, by the concentrations of elements in solid solution. Additions of manganese, chromium, and zirconium are made to a wide variety of alloys because the dispersions of particles that can be developed are useful for inhibiting the development and growth of new grains during recrystallization (Fig. 56). Inhibiting the growth of new grains can, under appropriate conditions, allow a fine grain size to develop; by delaying the growth of the first few grains that nucleate, other nuclei are afforded the time to develop.

If a sufficiently high volume fraction of suitable dispersoid particles can be generated, discontinuous recrystallization can be strongly inhibited. Alloys with such a microstructure have been developed and have a useful combination of formability and strength (Fig. 57). In the aluminum-calcium-zinc alloy of this type, a high volume fraction of fine particles can be achieved. This alloy has excellent superplastic particles.

In several important alloy systems, including aluminum-copper (2XXX), aluminum-magnesium-silicon (6XXX), and aluminum-zinc-magnesium

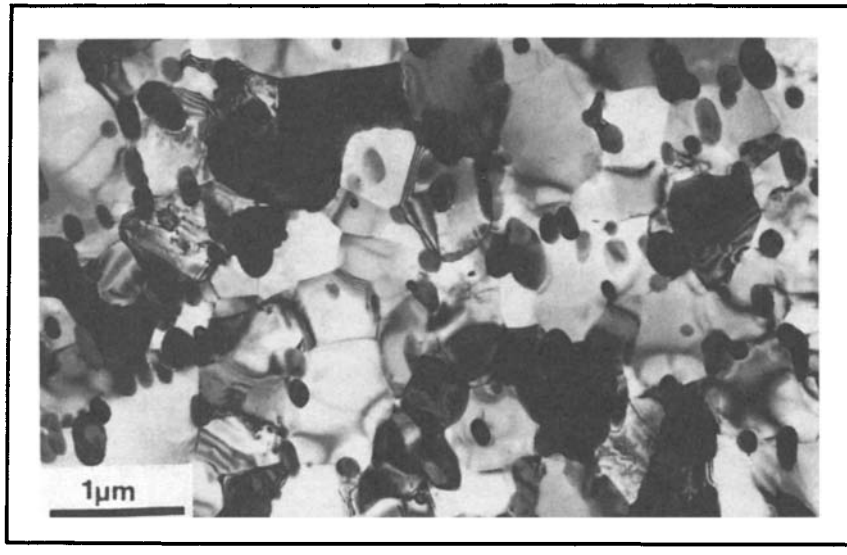

Fig. 57. An ultrafine grain size, particle-stabilized microstructure (×7125). (Courtesy of Alcan International Ltd.)

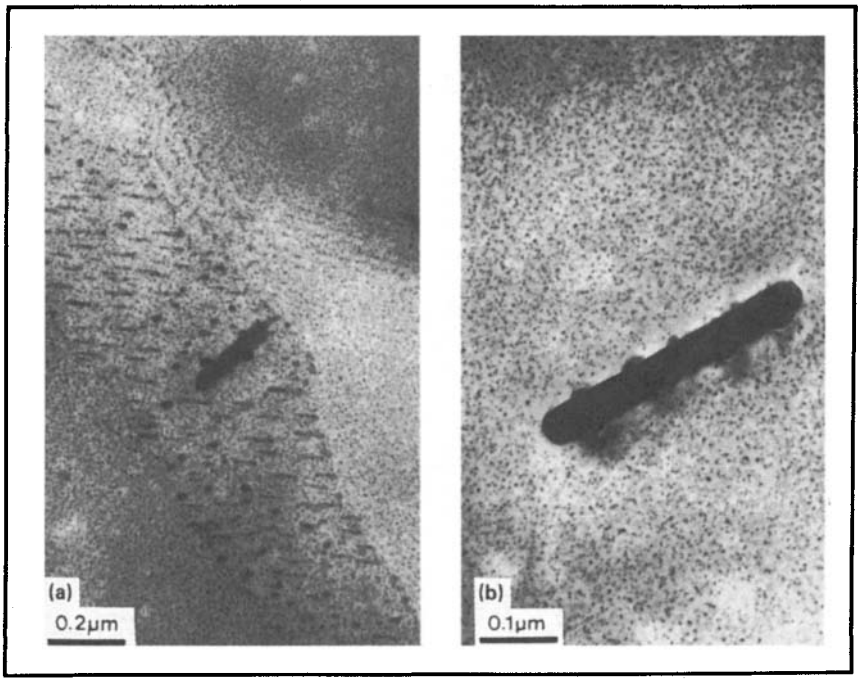

Fig. 58. Precipitation of $MgZn_2$ at heterogeneous sites: (a) on subgrain boundaries; and (b) on a manganese-bearing dispersoid particle. (Courtesy of Alcan International Ltd.)

(7XXX), the heat treatments that are normally used are designed to produce a very high density of fine GP zones or precipitates that strongly interact with dislocations and thereby increase the yield strength of the alloy. A typical heat treatment program for these alloy systems consists of an initial solution heat treatment, which dissolves particular alloying elements. This is followed by quenching, which is designed to retain a high level of the dissolved elements in supersaturated solid solution. In this condition, the alloy can be given an aging heat treatment to achieve the required temper, although for some alloys, particularly the aluminum-zinc-magnesium (7XXX) series, significant improvements in properties occur during a period of natural (room temperature) aging.

Microstructural changes that occur during quenching and aging treatments of these alloy systems have been extensively studied using TEM. During quenching of the solution treated alloy, dislocations and precipitates can develop. These dislocations generally appear as helices, loops, or tangles generated as a result of quenching strains and the condensation of excess vacancies. Dislocation density depends on the solution treatment temperature and the levels of elements in solution, as these factors affect vacancy concentration. Quench rate also is important, because this determines the temperatures and times during which the vacancies are

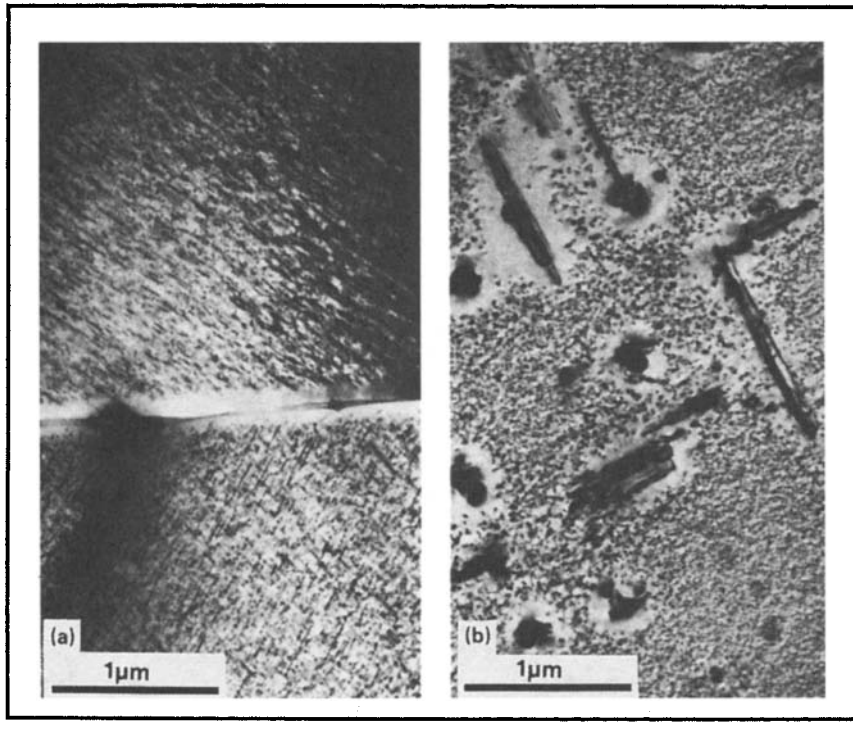

Fig. 59. Precipitate-free zones in samples that have been solution treated, slowly quenched, and then aged. (a) At a grain boundary in a 6XXX alloy. (b) Around manganese-bearing dispersoid particles in a 7XXX alloy. (Courtesy of Alcan International Ltd.)

mobile. Dislocations are also generated at constituent or dispersoid particles. These dislocations are produced by the differential contraction that occurs during the quench.

Ideally, to obtain maximum age hardening, all the dissolved elements should be retained in solid solution during the quench. This can be achieved by very rapid quenching, but in many commercial situations this is not possible, and lower cooling rates are used. As the cooling rate decreases, precipitate particles are found in increasing numbers. These precipitates nucleate at heterogeneous sites such as grain boundaries, dislocations, or on dispersoid particles. The most advantageous sites are populated first (Fig. 58). Thus, some grain boundaries, because of their misorientation, offer more favorable precipitate nucleation sites than others, and similarly some dislocations are preferred because of their edge or screw character. As well as acting as favorable nucleation sites for precipitation during quenching, subsequent aging reveals precipitate-free zones having widths related to the rate of quenching (Fig. 59a).

The presence of dispersoid particles in an alloy can substantially affect this quench-sensitive precipitation, partly because they modify the dis-

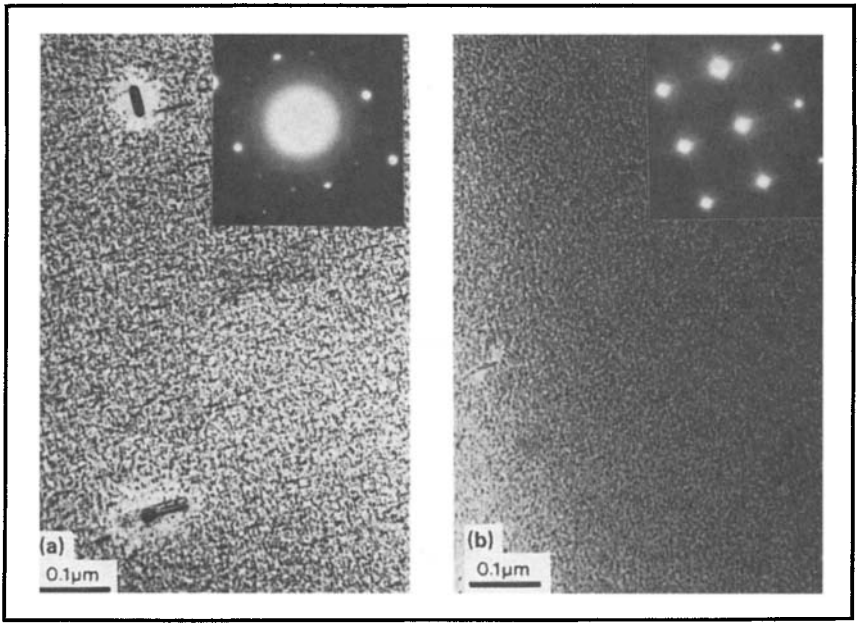

Fig. 60. Examples of heat treatable alloys that have been overaged to show the precipitates. (a) 6XXX alloy; needle-like β-Mg_2Si precipitates growing in $[100]_{Al}$ directions. The extra spots and streaks in the diffraction pattern are because of the precipitates and the associated strain fields. (b) An Al-4% Cu alloy; platelike θ′ precipitates arranged on $\{200\}_{Al}$ planes. The precipitates and strain fields again result in streaking in the diffraction pattern. (Courtesy of Alcan International Ltd.)

location structure of the quenched material. Also, dispersoid particles act as nucleation sites for precipitation in their own right (Fig. 59b). Manganese- and chromium-bearing phases are particularly potent dispersoids and readily nucleate precipitates during quenching, whereas coherent $ZrAl_3$ particles are less active nucleation sites.

During artificial aging, the elements in supersaturated solution begin to precipitate, and the strength of the material increases as the number and size of the precipitates increases. Eventually, the strength reaches a maximum value (the peak aged condition), and any further overaging leads to coarsening of the precipitates and a reduction in properties.

During age hardening, the precipitation phenomena that are observed can be quite complicated, and often several intermediate phases are involved. For example, in an aluminum-copper (2XXX) alloy, aging normally starts with the development of very fine plate-like GP zones in the matrix, on {001} planes. At this stage, GP zones are about 10 nm (100 Å) in diameter and consist of single planes of copper atoms. As aging proceeds, the GP zones transform to a coherent θ″ phase. Further aging results in successive transformation to semicoherent θ′ and eventually to plate-like particles of θ-$CuAl_2$. The aging kinetics and to some extent the precipitation sequence depend on the diffusion of copper atoms and is

influenced by the levels of vacancies and also the presence of traces of certain elements such as cadmium, indium, or tin that interact with the vacancies.

During the aging of aluminum-zinc-magnesium (7XXX) alloys, small spherical zones develop. As particles coarsen, they grow in preferred crystallographic orientations, and an overaged structure consists of elongated precipitates. Crystallographically distinct phases have been detected in these alloys including η', x, t, and η phases. The aging kinetics and the types of precipitate that are preferred are again influenced by the presence of trace elements. For example, a very low level of silver (<0.1 at.%) significantly accelerates the aging process. Aging of aluminum-magnesium-silicon (6XXX) alloys involves the nucleation and growth of rods of Mg_2Si that grow in [002], as shown in Fig. 60.

REFERENCES

1. Microstructure of Aluminum Alloys, *Metals Handbook, Atlas of Microstructures of Industrial Alloys,* 8th ed., Vol 7, American Society for Metals, 1972, p 242-272
2. Metallographic Technique for Aluminum Alloys, *Metals Handbook, Metallography, Structures and Phase Diagrams,* 8th ed., Vol 8, American Society for Metals, 1972, p 120-129
3. L.F. Mondolfo, *Aluminum Alloys—Structure & Properties,* Boston: Butterworths, 1976
4. R.W. Hertzberg, *Deformation and Fracture Mechanics of Engineering Material,* New York: John Wiley & Sons, 1976
5. J. Iglessis, C. Frantz, and M. Gantois, *Memoires Scientifique de la Revue de Metallurgie,* Vol 73, 1977, p 237
6. J. Iglessis, C. Frantz, and M. Gantois, *Memoires Scientifique de la Revue de Metallurgie,* Vol 74, 1978, p 93
7. H. Elias, Ed., *Stereology,* New York: Springer-Verlag, 1967
8. J.E. Vruggink, *Metals Engineering Quarterly,* Vol 49 (No. 9), Aug 1974, p 3-8
9. P.V. Blau, *Metallography,* Vol 9, 1976, p 257-271
10. D.S. Thompson, Metallurgical Factors Affecting High Strength Aluminum Alloy Production, *Metallurgical Transactions A,* Vol 6A, 1975, p 671
11. G.T. Hahn and A.R. Rosenfeld, Metallurgical Factors Affecting Toughness of Aluminum Alloys, 5th annual AIME meeting, May 1973
12. J.T. Staley, How Microstructure Affects Fatigue and Fracture of Aluminum Alloys, *Fracture Mechanics,* 1979, p 671-684
13. J.I. Goldstein and H. Yakowitz, Eds., *Practical Scanning Electron Microscopy,* New York: Plenum Press, 1975

SELECTED REFERENCES

- J.W. Edington, *Practical Electron Microscopy in Materials Science* (series of five monographs), London: Macmillan, 1976
- P.B. Hirsch, *et al, Electron Microscopy of Thin Crystals,* London: Butterworths, 1971
- J.W. Martin and R.D. Doherty, *Stability of Microstructure in Metallic Systems,* London: Cambridge University Press, 1976